frontiers in Earth Science

ORIGINAL RESEARCH
published: 22 June 2021
doi: 10.3389/feart.2021.673063

Serpentinization-Driven H_2 Production From Continental Break-Up to Mid-Ocean Ridge Spreading: Unexpected High Rates at the West Iberia Margin

Elmar Albers[1]*, *Wolfgang Bach*[1,2], *Marta Pérez-Gussinyé*[1,2], *Catherine McCammon*[3] and *Thomas Frederichs*[1,2]

[1]MARUM – Center for Marine Environmental Sciences, University of Bremen, Bremen, Germany, [2]Department of Geosciences, University of Bremen, Bremen, Germany, [3]Bayerisches Geoinstitut, University of Bayreuth, Bayreuth, Germany

Molecular hydrogen (H_2) released during serpentinization of mantle rocks is one of the main fuels for chemosynthetic life. Processes of H_2 production at slow-spreading mid-ocean ridges (MORs) have received much attention in the past. Less well understood is serpentinization at passive continental margins where different rock types are involved (lherzolite instead of harzburgite/dunite at MORs) and the alteration temperatures tend to be lower (<200°C vs. >200°C). To help closing this knowledge gap we investigated drill core samples from the West Iberia margin. Lherzolitic compositions and spinel geochemistry indicate that the exhumed peridotites resemble sub-continental lithospheric mantle. The rocks are strongly serpentinized, mainly consist of serpentine with little magnetite, and are generally brucite-free. Serpentine can be uncommonly Fe-rich, with X_{Mg} = Mg/(Mg + Fe) < 0.8, and shows distinct compositional trends toward a cronstedtite endmember. Bulk rock and silicate fraction Fe(III)/∑Fe ratios are 0.6–0.92 and 0.58–0.8, respectively; our data show that 2/3 of the ferric Fe is accounted for by Fe(III)-serpentine. Mass balance and thermodynamic calculations suggest that the sample's initial serpentinization produced ~120 to >300 mmol H_2 per kg rock. The cold, late-stage weathering of the serpentinites at the seafloor caused additional H_2 formation. These results suggest that the H_2 generation potential evolves during the transition from continental break-up to ultraslow and, eventually, slow MOR spreading. Metamorphic phase assemblages systematically vary between these settings, which has consequences for H_2 yields during serpentinization. At magma-poor rifted margins and ultraslow-spreading MORs, serpentine hosts most Fe(III). Hydrogen yields of 120 to >300 mmol and 50–150 mmol H_2 per kg rock, respectively, may be expected at temperatures of <200°C. At slow-spreading MORs, in contrast, serpentinization may produce 200–350 mmol H_2, most of which is related to magnetite formation at >200°C. Since, in comparison to slow-spreading MORs, geothermal gradients at magma-poor margins

OPEN ACCESS

Edited by:
Michel Grégoire, Centre National de la Recherche Scientifique (CNRS), France

Reviewed by:
Othmar Müntener, University of Lausanne, Switzerland
Costanza Bonadiman, University of Ferrara, Italy

***Correspondence:**
Elmar Albers
e.albers@uni-bremen.de

Specialty section:
This article was submitted to Petrology, a section of the journal Frontiers in Earth Science

Received: *26 February 2021*
Accepted: *03 June 2021*
Published: *22 June 2021*

Citation:
Albers E, Bach W, Pérez-Gussinyé M, McCammon C and Frederichs T (2021) Serpentinization-Driven H_2 Production From Continental Break-Up to Mid-Ocean Ridge Spreading: Unexpected High Rates at the West Iberia Margin. Front. Earth Sci. 9:673063. doi: 10.3389/feart.2021.673063

Abbreviations: Amp, amphibole; Cb, carbonate; Cpx, clinopyroxene; Mt, magnetite; Opx, orthopyroxene; Spl, spinel; Srp, serpentine; LOI, loss on ignition; SD, standard deviation; b.d.l., below detection limit.

and ultraslow-spreading MORs are lower, larger volumes of low-temperature serpentinite should form in these settings. Serpentinization of lherzolitic rocks at magma-poor margins should produce particularly high amounts of H_2 under conditions within the habitable zone. Magma-poor margins may hence be more relevant environments for hydrogenotrophic microbial life than previously thought.

Keywords: serpentinization, hydrogen generation, magma-poor rifted margin, mid-ocean ridges, ultraslow spreading, hydrothermal alteration, chemosynthetic life, seafloor weathering

INTRODUCTION

Serpentinites in the oceanic lithosphere form when mantle peridotite interacts with seawater at temperatures below ~450°C. A byproduct of this reaction is molecular hydrogen (H_2), which in turn provides a source of metabolic energy for lithoautotrophic microbial communities (e.g., Sleep et al., 2004; Edwards et al., 2005; Petersen et al., 2011). Serpentinization sites have hence repeatedly been proposed as locations favorable for life to have evolved on Earth and elsewhere (e.g., Schulte et al., 2006; McCollom and Seewald, 2013; Fryer et al., 2020). The understanding of serpentinization-related H_2 production has been of great interest over the last years.

Major sites of serpentinization—and thus of H_2 production—are slow and ultraslow-spreading mid-ocean ridges (MORs) and magma-poor rifted margins, where mantle peridotite is frequently exposed to the seafloor by tectonic processes (e.g., Brun and Beslier, 1996; Cannat et al., 2010; Sauter et al., 2013). Serpentinization reactions and the associated H_2 formation at MORs have been extensively investigated in the past (e.g., Bach et al., 2006; Klein et al., 2009; Andreani et al., 2013; Tutolo et al., 2020). The hydration of mantle peridotite by seawater leads to the oxidation of ferrous Fe in primary minerals, i.e., olivine and pyroxene, to Fe(III) in secondary phases, following the generalized reaction $2\ FeO + H_2O = Fe_2O_3 + H_2(aq)$ (e.g., Sleep et al., 2004). Major hosts of ferric Fe are magnetite, $Fe_2^{3+}Fe^{2+}O_4$, and the Fe^{3+}-serpentine varieties hisingerite, $Fe_2^{3+}Si_2O_5(OH)_4$, and cronstedtite $(Mg,Fe^{2+})_2Fe_2^{3+}SiO_5(OH)_4$. Magnetite is most abundant at temperatures of 200–350°C, causing the production of >300 mmol H_2 per kg of dunite or harzburgite at these temperatures, but its abundance decreases toward lower temperatures at which Fe is progressively incorporated into Fe-rich brucite (Bach et al., 2006; Klein et al., 2009). At such lower temperatures, Fe(III)-serpentine is the main host for ferric Fe and the total amounts of H_2 produced are thought to be much lower (below ~100 mmol per kg of rock; Klein et al., 2009; Andreani et al., 2013).

Serpentinization processes at magma-poor margins have received less attention. The chemical compositions of mantle rocks in these settings, however, commonly differ from peridotites at MORs. Specifically, rocks in ocean–continent transition (OCT) zones have experienced only moderate degrees of melt depletion and are hence compositionally closer to sub-continental lithospheric mantle (SCLM). Such rocks contain higher modal amounts of pyroxene than peridotite at MORs and thus more Si, Al, Ca, and Na (e.g., Hébert et al., 2001; Bodinier and Godard, 2014). Owing to these differences in bulk composition, serpentinization pathways likely differ from those at MORs where generally more depleted peridotites are serpentinized. For instance, higher Si in the bulk system potentially reduces the amount of brucite being formed (cf. Frost and Beard, 2007). Instead, more serpentine may form, some of which may hold Fe(III), which itself would increase the rates of H_2 production (see, e.g., reviews by Evans et al., 2013; Mayhew and Ellison, 2020).

The most prominent example of a magma-poor margin is the one at West Iberia, which formed during the break-up of Pangaea. Here, continental rifting caused thinning of the crust and eventually the widespread exposure of lithospheric mantle peridotite to the young North Atlantic Ocean seafloor (e.g., Boillot et al., 1988; Pickup et al., 1996; Pérez-Gussinyé, 2012). These exposures include the OCT, i.e., exhumed mantle that ranges in composition from weakly depleted sub-continental lherzolite to more depleted harzburgitic/dunitic rocks in the oceanic lithosphere (e.g., Hébert et al., 2001; Chazot et al., 2005). Studies of serpentinization at the West Iberia margin have mostly focused on peridotites from the depleted oceanic-type mantle (Sites 897 and 899 drilled during Ocean Drilling Program (ODP) Leg 149, and Sites 1067, 1068, and 1070 of Leg 173; e.g., Beard and Hopkinson, 2000; Skelton and Valley, 2000; Hopkinson et al., 2004; Schwarzenbach et al., 2013). To our knowledge, there are no detailed investigations on the serpentinization of the more continental-type mantle exposures—these reactions hence remain incompletely understood.

In this work we investigate serpentinization processes and the associated production of H_2 in pyroxene-rich mantle peridotite from the OCT at the West Iberia margin. By discussing the effects of bulk rock composition, spreading velocities, and temperature conditions during alteration, this study outlines the systematic changes in serpentinization reaction pathways and H_2 yields during the evolution from continental break-up to mid-ocean ridge divergence at ultraslow and eventually slow spreading rates.

Geological Setting and Samples

The West Iberia margin is a hyperextended magma-poor margin that documents the break-up of Pangaea and the early stages of the opening of the North Atlantic. Combined seismic studies and oceanic research drilling (ODP Legs 103, 149, and 173) have revealed the evolution from thinned continental crust over the OCT to purely oceanic crust (e.g., Boillot et al., 1987; Manatschal et al., 2001; Pérez-Gussinyé and Reston, 2001; Whitmarsh et al., 2001; Reston and McDermott, 2011; Dean et al., 2015). The OCT

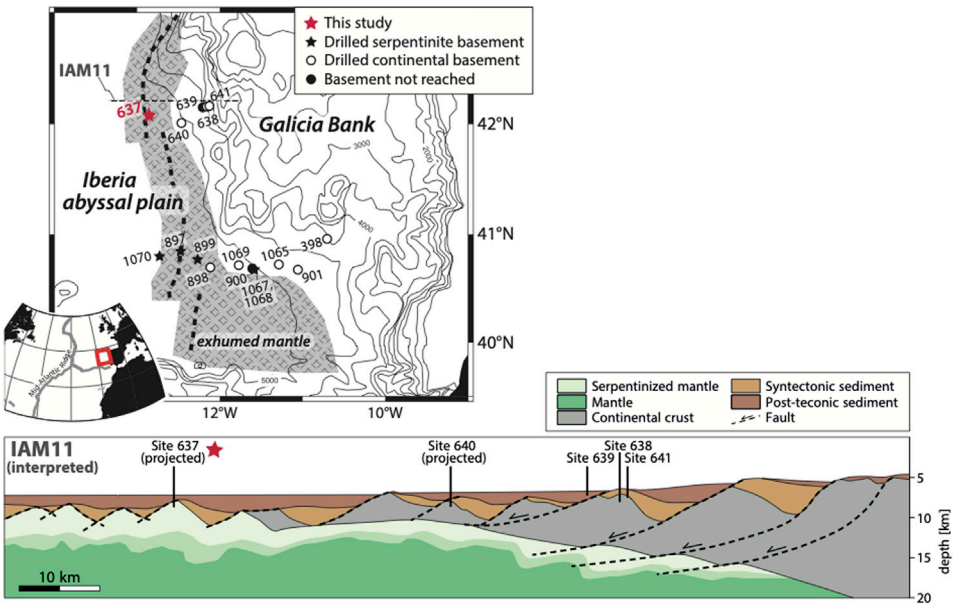

FIGURE 1 | Simplified map of and geological cross section across the West Iberia margin. Indicated are the approximate extent of peridotite exhumed to the seafloor and the drill site locations of ODP Legs 103, 149, and 173. Samples investigated here originate from Site 637, which represents the most landward domain of the OCT. The other drill sites are located in structural positions further oceanward. Map after Whitmarsh and Wallace (2001) and Klein et al. (2015), structural interpretation of seismic line IAM11 after Ranero and Pérez-Gussinyé (2010).

is about 40–170 km wide and consists of several north–south-trending "peridotite ridges" at which lithospheric mantle has been exhumed to the seafloor along a series of extensional faults (**Figure 1**; see references above). The extension that lead to this mantle exhumation took place at rates of ~10 mm/yr (Whitmarsh and Miles, 1995). The peridotites are generally characterized by variable degrees of melt depletion, in concert with the evolution from sub-continental to oceanic lithospheric mantle (e.g., Abe, 2001; Hébert et al., 2001; Chazot et al., 2005). Seawater influx along numerous extensional faults led to extensive serpentinization of the ultramafic rocks. Up to 100% of the peridotite has been transformed into serpentinite to a depth of ~4 km below the seafloor, as evidenced by drill cores and suggested by seismic imaging (e.g., Boillot et al., 1988; Dean et al., 2000; Beslier et al., 2001; Bayrakci et al., 2016). At even greater depths, serpentinites may account for up to 25% of the basement, in particular where deep faults are present (e.g., Dean et al., 2000). The timescales for serpentinization were estimated to be ~10^5–10^6 years (Skelton et al., 2005) even though some hydration of the uppermost mantle may have taken place before its exhumation (Skelton and Valley, 2000; Pérez-Gussinyé and Reston, 2001; Pérez-Gussinyé et al., 2006). The bulk of the serpentinization took place at temperatures of 120–200°C (Agrinier et al., 1988; Agrinier et al., 1996; Schwarzenbach et al., 2013; Klein et al., 2014).

The rock samples investigated here originate from ODP Leg 103, Hole 637A—a drill site within the transition from SCLM to oceanic mantle at the Galicia Bank (**Figure 1**). Coring extended ~75 m into the basement and recovered dominantly clinopyroxene-rich spinel harzburgites and lherzolites (Boillot et al., 1988). The rocks are rich in Na, Al, and Ti, and spinel has particularly low Cr/Al and high Mg/Fe ratios, suggesting low degrees of depletion by melt extraction (<10%; Evans and Girardeau, 1988). The peridotites were likely exposed to the seafloor prior to the establishment of seafloor spreading (Evans and Girardeau, 1988). They are strongly serpentinized with dominantly pervasive replacement textures (Boillot et al., 1988). Shallow within the drill hole, the serpentinites have a leached appearance and replacement by calcite is common; further downcore, calcite is rather present in veins (Evans and Baltuck, 1988). Our samples originate from ~230 to 267 m below the seafloor.

METHODOLOGY

Polished thin sections were examined with a standard petrographic microscope. Primary and secondary fabrics and mineral phase assemblages and compositions were further evaluated on the basis of backscattered electron (BSE) imaging, energy-dispersive X-ray spectroscopy, and electron microprobe analyses. For bulk rock investigations, 10–15 g of sample were homogenized and aliquots of these were used for the different analyses. Sample preparation included cutting with a rock saw, cleaning with deionized water in an ultrasonic bath, and drying of the samples at 50°C. The samples were pulverized using a planetary agate ball mill.

Bulk Rock Elemental Analyses

Bulk rock compositions were analyzed on fused glass beads at the Institute for Chemistry and Biology of the Marine Environment at the University of Oldenburg. Preparation included the preoxidation and melting of weighed portions of sample, $Li_2B_4O_7$ and NH_4NO_3 at 500 and 1,450°C, respectively, following Eckert et al. (2013). Concentrations of major and trace element concentrations were measured with a wavelength dispersive PANalytical Axios plus X-ray fluorescence spectrometer. Analyses of in-house reference materials were used to monitor the data quality. Analytical accuracies are better than 2.6% for major elements, except for Na_2O.

Carbon contents were measured on a LECO CS744 combustion analyzer at the Department of Geosciences, University of Bremen. Contents of total carbon were determined on ~0.1 g dried bulk rock powder, and contents of total organic carbon were analyzed on ~0.1 g aliquots of rock powder that were previously treated with HCl (12.5%) to remove all inorganic carbon. Amounts of total inorganic carbon were calculated by subtracting total organic carbon from total carbon contents.

Magnetometry and Saturation Magnetization

For measurement of magnetic hysteresis, between 20 and 30 mg of sample powder were filled into a plastic straw and then hardened by applying a small amount of glue (cyanoacrylate). Measurements were performed at the Department of Geosciences, University of Bremen, on a Princeton Measurement Corporation Micromag 2,900 Alternating Gradient Magnetometer (Flanders, 1988). The accuracy of the instrument is 2% vs. the calibration sample (77.67×10^{-6} Am^2, standard reference material 2,853, Yttrium Iron Garnet); its sensitivity is 10×10^{-12} Am^2 standard deviation. The maximum applied fields were 0.3 and 1 T, respectively, which are sufficient to saturate magnetite; hematite and goethite need much larger field strengths to become magnetically saturated. The saturation magnetization of magnetite, hematite, and goethite are 480, ~2.5 and ~2 kA m^{-1}, respectively (Dunlop and Özdemir, 1997). These numbers result in specific magnetizations of 92.36, 0.47, and 0.47 Am^2 kg^{-1} when applying densities of 5.197, 5.271 and 4.264 g cm^{-3}, respectively (Dunlop and Özdemir, 1997). After conducting the magnetic hysteresis measurements, we subtracted the linear slope from the data calculated for the field interval larger than 70% of the peak field, which is due to para- and/or diamagnetic constituents.

We estimated magnetite concentrations by assuming that it contributes the largest part to the saturation magnetization of the entire sample, also in the presence of other Fe oxides or hydroxides, due to its ~200 times higher specific magnetization compared to hematite and goethite. (Partial) oxidation of magnetite, although decreasing its mass magnetization, would not dramatically affect the computed magnetite concentrations, because the mass magnetization of fully oxidized maghemite (γ-Fe_2O_3) is still 74.89 Am^2 kg^{-1} (Dunlop and Özdemir, 1997).

Fe(III)/∑Fe Analyses

In order to further examine possible oxidation of the magnetic mineral phases we exemplarily performed temperature-dependent remanence measurements and additional magnetic hysteresis measurements in peak fields of 1 T on two samples (25R-4 and 27R-2, 126–130 cm). The relative sensitivity of the used Quantum Design MPMS XL-7 superconducting quantum interference device (SQUID) magnetometer operated at the University of Bremen is $<1 \times 10^{-11}$ Am^2. An isothermal remanent magnetization was imparted to the samples in a steady magnetic field of 5 T at 300K. Afterward, the sample was cooled in zero-field to 5K and subsequently re-warmed to 300K (cf. Özdemir and Dunlop, 2010).

Fe(III)/∑Fe was determined for all samples using Mössbauer spectroscopy at Bayerisches Geoinstitut, University of Bayreuth. Roughly 200 mg of each sample were mounted in plastic holders, which corresponds to a Mössbauer thickness of 13 mg Fe cm^{-2}. Mössbauer spectra were recorded at room temperature in transmission mode on a constant acceleration Mössbauer spectrometer with a nominal 1.85 GBq ^{57}Co source in Rh. The velocity scale was calibrated relative to metallic iron. Spectra were collected for between one and five days and fit using MossA software (Prescher et al., 2012). Iron-containing phases could be identified based on hyperfine parameter values, and the distribution of Fe between phases was calculated from relative areas.

Electron Microprobe Analyses

Mineral chemical compositions were obtained with a CAMECA SX100 microprobe at the Department of Geosciences, University of Bremen. The device is equipped with four wavelength dispersive spectrometers. Analytical conditions included accelerating voltages of 15 kV and beam currents of 10–20 nA. Peak counting times varied between 20 and 40 s per element; analyses of primary phases were carried out with a focused beam whereas alteration phases were measured with a beam of 5 µm diameter. The built-in PAP correction was applied for data reduction and correction. Natural silicate and oxide standards (olivine, USNM 143965, number of analyses, n = 25; hornblende, USNM 143965, n = 20; chromite, USNM 117075, n = 22; Jarosewich et al., 1980) were repeatedly analyzed to check data quality. For elements with concentrations >1 wt%, the external reproducibility is better than 2.5%, except for Na_2O (3.2%), and the averaged relative error as a measure for accuracy is below 2.5%, except for TiO_2 (3.2%) and Na_2O (6.5%).

Thermodynamic Calculations

Modeling was conducted using EQ3/6 version 8.0 (Wolery and Jarek, 2003) and the customized database from Klein et al. (2013), which has been assembled using SUPCRT92 (Johnson et al., 1992). The database contains log K values for temperatures from 0 to 400°C in 25°C increments at a constant pressure of 50 MPa. Details of thermodynamic data and on the calculation of activity coefficients in the database can be found in Klein et al. (2013). The models include solid solutions for olivine (forsterite, fayalite), orthopyroxene (enstatite, ferrosilite), clinopyroxene (diopside, hedenbergite), serpentine (containing the endmembers

TABLE 1 | Overview of investigated samples, estimated protolith type, degree of alteration, internal classification of the alteration state (cf. *Iron Oxidation State and Magnetite Contents*), and phase assemblages.

Sample	Depth (mbsf)	Protolith[a]	% Altered	Category	Cpx	Opx	Spl	Srp[b]	Amp	Mt	Cb	Abbreviated sample name
637A-25R-2, 62–65 cm	230.12	lherzolite	91	Oxidized	x	x	x	x		x	x	25R-2
637A-25R-3, 10–13 cm	231.10	Harzburgite	94	Oxidized	x	x	x	x		x	x	25R-3
637A-25R-4, 28–32 cm	232.78	Harzburgite	92	Oxidized	x	x	x	x		x	x	25R-4
637A-25R-5, 119–122 cm	235.19	Harzburgite	89	Oxidized	x	x	x	x		x	x	25R-5
637A-26R-3, 66–69 cm	240.86	Dunite	100	Metasomatized			x	x		x	x	26R-3
637A-27R-1, 45–48 cm	247.35	lherzolite	97	Metasomatized	x		x	x	x	x	x	27R-1, 45–48 cm
637A-27R-1, 107–110 cm	247.97	lherzolite	94	Oxidized	x	x	x	x	x	x	x	27R-1, 107–110 cm
637A-27R-1, 147–150 cm	248.37	lherzolite	96	Least modified	x	x	x	x	x	x		27R-1, 147–150 cm
637A-27R-2, 65–68 cm	249.05	lherzolite	94	Least modified	x	x	x	x	x	x	x	27R-2, 65–68 cm
637A-27R-2, 126–130 cm	249.66	lherzolite	91	Least modified	x	x	x	x	x	x	x	27R-2, 126–130 cm
637A-27R-4, 75–79 cm	252.15	Harzburgite	91	Least modified	x	x	x	x	x	x	x	27R-4
637A-28R-1, 138–141 cm	257.98	lherzolite	99	Metasomatized	x	x	x	x		x	x	28R-1
637A-28R-3, 68–70 cm	260.28	Harzburgite	100	Metasomatized			x	x		x		28R-3
637A-28R-4, 36–40 cm	261.46	Harzburgite	100	Metasomatized				x		x		28R-4
637A-29R-1, 36–39 cm	266.69	Harzburgite	96	Metasomatized	x		x	x		x	x	29R-1

[a]*Estimated based on point-counting of modal amounts of olivine and its alteration product (mesh serpentine) vs. pyroxene and its alteration product (serpentine in bastite textures).*
[b]*Including solid solutions with and/or intergrown amesite, cronstedtite, talc, and stevensite.*

chrysotile, greenalite, kaolinite, and cronstedtite, to allow substitution of ferric Fe at the tetrahedral and octahedral sites), brucite (Mg-brucite and ferroan brucite), talc (talc, minnesotaite), chlorite (clinochlore, daphnite), and tremolite (tremolite, Fe-actinolite). All solid solutions were allowed to vary freely over their entire compositional range, with the exception of olivine, the composition of which was fixed at X_{Mg} = Mg/(Mg + Fe) of 0.90 (cf. McCollom and Bach, 2009). Metastable equilibria were accounted for by suppressing the formation of antigorite, aragonite, calcite, dolomite, huntite, hydroxyltopaz, magnesite, and monticellite during all model runs. In the first set of models (described below), the formation of garnet was also suppressed since we did not observe garnet in our samples. However, garnet has been described from other West Iberia peridotites (e.g., Beard and Hopkinson, 2000) and we performed a second round of modeling that allowed for its formation.

The calculations were done in three steps that mimic the inflow of seawater into peridotite basement, changes in fluid chemistry during the reaction with the basement, and the eventual serpentinization of peridotite by the seawater-derived fluid. We first speciated 1 kg of sulfate-free, seawater-like fluid (composition as in Table 3 of Klein et al. (2009)), except that we excluded HCO_3^- and SO_4^{2-}), at 25°C and 50 MPa using EQ3NR. In the second step, 1 kg of solid reactant was added in increments to the seawater and equilibrated for the same conditions using EQ6. We chose two rock compositions as solid reactants: 1) sample 25R-2 as an example for rocks from the OCT; 2) an undepleted hypothetical endmember composition (Salters and Stracke, 2004). In the last modeling step, the system was heated to 400°C in small increments and equilibrated at each step, also using EQ6. All calculations were performed for a pressure of 50 MPa, representing shallow to intermediate crustal depths (~1.5–2 km). This modeling approach allows determining the equilibrium compositions for the bulk system during hydration at an initial water-to-rock (w/r) mass ratio of unity, and the mineral and fluid compositions as a function of temperature. Such a w/r ratio is thought to prevail during pervasive serpentinization (cf. Barnes and Sharp, 2006) and is likely representative for the hydration of the investigated samples. Further, the calculated equilibrium assemblages/conditions are well representative of the West Iberia margin samples since serpentinization reactions proceed relatively fast and local equilibria have likely been reached throughout most of the samples. In addition, a set of calculations for a w/r ratio of 10 was performed to investigate the higher fluxes that may have prevailed active fault zones.

RESULTS

Petrography

The fifteen samples are strongly serpentinized lherzolites and harzburgites, and one dunite. An overview of the samples, the presumed protolith types, and the degree of alteration is presented in **Table 1**.

Protolith fabrics were mostly overprinted during serpentinization. Where preserved, they can differ on a centimeter scale (**Figures 2A,B**). In some samples, deformation of peridotite is illustrated by elongated pyroxene and Cr spinel grains (e.g., samples 25R-3 and 29R-1) and in some cases by foliation or brittle deformation textures (e.g., sample 27R-1, 147–150 cm). Other samples lack such deformation fabrics and instead show non-elongated pyroxene and/or Cr spinel (e.g., samples 28R-3 and 27R-4). Unaltered olivine was not observed but primary clinopyroxene, orthopyroxene, and spinel are locally present (**Figures 2A–C**). Pyroxene frequently shows undulatory extinction and cleavage planes. Clinopyroxene grains are usually up to ~2 mm long, but may reach lengths of >4 mm (e.g., sample 25R-5), and often occurs close to

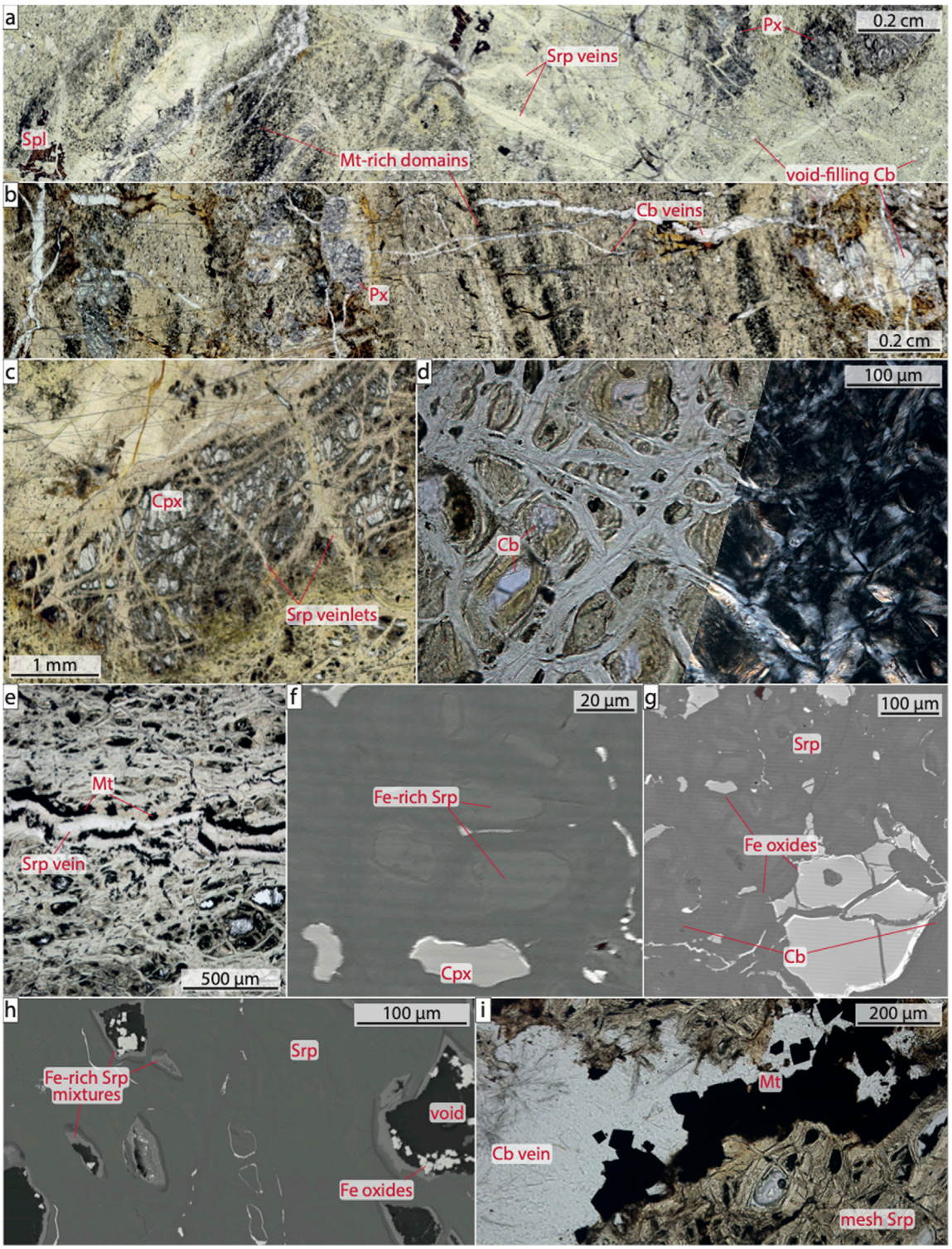

FIGURE 2 | Petrographic and textural features of the studied samples **(A)** Thin section scan showing a typical sample with domains of magnetite-poor serpentine mesh textures and darker domains enriched in magnetite. Pyroxene is partly and spinel is mostly unaltered. Light-colored serpentine veins crosscut previous textures. Carbonate fills voids, many of which may have been former mesh centers. Sample 27R-4, 75–79 cm, plane polarized light (PPL) **(B)** Thin section scan showing a domain rich in mostly unaltered pyroxene. Magnetite appears concentrated in elongated domains (dark areas). Carbonate veins crosscut the sample. Sample 25R-3, 10–13 cm, PPL **(C)** Photomicrograph depicting mostly unaltered clinopyroxene with some serpentine present along intragranular fractures. Sample 25R-5, 119–122 cm, PPL **(D)** Photomicrograph showing typical serpentinite mesh texture. Carbonate occurs in some mesh centers. Sample 27R-2, 126–130 cm, PPL (left)

(*Continued*)

FIGURE 2 | and crossed polarized light (right) **(E)** Photomicrograph of a narrow serpentine–magnetite vein crosscutting an extensively serpentinized sample. Sample 29R-1, 36–39 cm, PPL **(F)** BSE image of Fe-rich serpentine in mesh centers (light gray; X_{Mg} = 0.88) separated by Mg-rich intergranular serpentine (X_{Mg} = 0.93). Sample 27R-2, 126–130 cm **(G)** BSE image of euhedral magnetite in a serpentine vein. Sample 27R-1, 107–110 cm **(H)** BSE image showing voids within blocky serpentine, the inner walls of which are overgrown by Fe-rich serpentine–amesite–stevensite/talc mixtures (X_{Mg} = 0.65). Euhedral Fe oxides precipitated within the voids. Sample 29R-1, 36–39 cm **(I)** Photomicrograph of a carbonate vein with euhedral magnetite crosscutting serpentinite. Sample 25R-2, 62–65 cm, PPL. Abbreviations: Cb, carbonate; Cpx, clinopyroxene; Mt, magnetite; Px, pyroxene; Spl, spinel; Srp, serpentine.

orthopyroxene or in its exsolution lamellae (e.g., sample 25R-4). Orthopyroxene is more frequent than clinopyroxene and is mostly ~3–4 mm in size (e.g., sample 27R-2, 126–130 cm). Typically, pyroxene is serpentinized along cleavage planes and microcracks; only minor parts are unaltered (**Figures 2A–C**). Spinel occurs in anhedral or holly-leaf shapes (e.g., samples 27R-1, 147–150 cm, and 27R-4, respectively) with grain sizes of up to ~2.5 mm. Some grains are rimmed by or locally altered to magnetite.

The samples are extensively altered, with degrees of serpentinization generally ≫90% (**Table 1**). Whereas shallow samples appear yellowish–brownish, dark brown–greyish colors dominate further downhole. Secondary mineral assemblages include serpentine, carbonate, oxides, and minor chlorite and amphibole (**Figures 2A–I**). Serpentine, the dominant phase, has in most cases pervasively replaced primary minerals but also can be found as precipitates in veins crosscutting the rocks (**Figures 2A,D–F**). Despite the pervasive replacement of olivine, its pseudomorphs can usually only be identified with scanning electron microscopy (**Figure 2F**). Bastite serpentine textures, by contrast, are commonly well discernible using polarized light microscopy (e.g., sample 28R-3). Highly porous serpentine that appears to have grown in void space—which we interpret to represent dissolved centers of former olivine and/or serpentine—is frequent throughout all samples. Micrometer-sized Fe oxides, presumably magnetite, are distributed in serpentine that pervasively replaced olivine as well as in veins. In some cases, magnetite forms bands crosscutting serpentine (**Figure 2E**). Accumulations of magnetite cause a local dark-colored appearance of serpentine (**Figure 2B**). In veins, grains can be up to 50 μm large (**Figure 2G**). Magnetite is less common within altered pyroxene. Up to 20 μm large, euhedral Fe-oxide grains with stoichiometries matching that of magnetite can further occur within void space (**Figure 2H**) or within carbonate veins (**Figure 2I**; see below). In a few samples we observed chlorite, mostly in the direct vicinity of spinel (e.g., sample 29R-1). Minor amounts of amphibole are associated with fresh or altered pyroxene in the lherzolitic samples; amphibole is usually anhedral but shows needle-like shapes in a few instances (e.g., samples 27R-1, 45–48 cm and 27R-2, 126–130 cm). The majority of the samples experienced late-stage carbonation, with frequent calcite occurrences in millimetric to centimeter-wide veins (e.g., samples 25R-4 and 26R-3) and in the centers of former olivine grains (**Figure 2D**). In some samples, euhedral Fe and/or Mn oxide grains are enclosed by calcite or occur in between the carbonate and the host mineral (e.g., samples 27R-1, 45–48 cm, and 28R-3).

Bulk Rock Geochemistry

The serpentinites are characterized by variable major elemental concentrations, in particular SiO_2 (23.7–41.2 wt%), MgO (21.1–35.7 wt%), Fe_2O_3 (6.2–9.5 wt%), and CaO (0.7–21.5 wt%; **Supplementary Table S1**). Total inorganic carbon (TIC) ranges from 0.4 to 17.1 wt% and the loss on ignition (LOI) from 13.1 to 25.1 wt%. TIC and CaO strongly correlate with LOI and SiO_2 whereas MgO anticorrelates with CaO, TIC, and LOI, respectively.

The data imply that $CaCO_3$ was added to the peridotites, resulting in a strong dilution of some samples. To assess the peridotite geochemistry before the addition of $CaCO_3$ we back-calculated the bulk rock compositions assuming that all TIC is present in the form of $CaCO_3$. The corrected values are presented in **Table 2** and **Figure 3** (dry rock). Ratios of Al_2O_3/SiO_2 and MgO/SiO_2 average at 0.041 ± 0.013 (1 SD) and 0.89 ± 0.033, respectively.

Trace elemental compositions are similar to previously published data from the Iberia margin (e.g., Seifert and Brunotte, 1996; Hébert et al., 2001).

Iron Oxidation State and Magnetite Contents

Bulk rock Mössbauer analyses revealed considerable distinctions between the samples and provide a means to identify different Fe oxides. These results allow a subdivision of the samples into three groups (**Table 1** and **Supplementary Table S3**). In the first two groups, about 3/4 of all Fe is present within silicate phases, which we will refer to as "least modified" and "oxidized" from here on. The bulk of the remaining Fe is incorporated in magnetite in the least modified samples and in goethite and/or hematite in the oxidized samples. Within the third group, the "metasomatised" samples, silicates are markedly less dominant and instead, goethite and/or hematite can contain up to 4/5 and hence most of the Fe (on average 56% vs. 6% in the least modified and 20% in the oxidized samples). Mössbauer spectra are available in **Supplementary Figure S1** and hyperfine parameter values in **Supplementary Figure S2**.

Bulk rock oxidation states, i.e., $Fe(III)/\sum Fe$, calculated on the basis of these data are about 0.6–0.65 for the least modified samples, around 0.8 in the oxidized samples, and up to 0.93 in the metasomatized ones.

In line with these results, bulk magnetization analyses suggest magnetite as the dominant magnetic mineral in the least modified samples and significant partial oxidation in the oxidized group. In greater detail, magnetic hysteresis loops of samples from both groups (25R-4 and 27R-2, 126–130 cm, respectively) indicate the dominance of low-coercivity minerals such as magnetite

TABLE 2 | Corrected bulk rock geochemistry, Fe oxidation state, and magnetite contents of the Hole 637A samples.

		637A-25R-2, 62–65 cm	637A-25R-3, 10–13 cm	637A-25R-4, 28–32 cm	637A-25R-5, 119–122 cm	637A-26R-3, 66–69 cm	637A-27R-1, 45–48 cm	637A-27R-1, 107–110 cm	637A-27R-1, 147–150 cm	637A-27R-2, 65–68 cm	637A-27R-2, 126–130 cm	637A-27R-4, 75–79 cm	637A-28R-1, 138–141 cm	637A-28R-3, 68–70 cm	637A-28R-4, 36–40 cm	637A-29R-1, 36–39 cm
SiO_2	wt%	45.14	44.05	44.72	46.23	41.62	45.29	45.97	46.58	46.35	47.55	45.25	42.36	44.78	38.62	43.64
TiO_2		0.09	0.06	0.05	0.07	0.01	0.02	0.02	0.02	0.06	0.05	0.06	0.04	0.16	0.27	0.07
Al_2O_3		2.62	1.66	2.55	2.42	0.84	1.05	1.73	1.25	2.18	1.41	2.33	1.42	2.06	1.61	2.47
Fe_2O_3		8.34	8.67	8.53	8.73	12.77	7.85	8.35	9.08	8.52	8.63	8.09	9.01	9.21	10.77	10.82
MnO		0.09	0.08	0.08	0.10	0.32	0.17	0.08	0.08	0.08	0.07	0.08	1.32	0.10	0.24	0.10
MgO		38.85	37.70	39.92	39.34	38.99	40.79	40.20	41.00	40.63	40.74	41.06	36.90	40.20	34.35	42.50
CaO		2.65	5.12	1.81	1.19	3.00	2.73	1.47	0.61	0.85	0.84	0.64	4.61	<0.03	7.14	<0.03
Na_2O		0.32	0.35	0.31	0.28	0.24	0.23	0.26	0.13	0.18	0.18	0.19	0.29	0.36	0.34	0.10
K_2O		0.09	0.12	0.05	0.04	0.01	0.03	0.04	0.01	0.02	0.01	0.03	0.03	0.03	0.05	0.01
Sum		83.70	81.19	84.48	85.22	82.03	83.53	84.21	86.53	86.20	87.34	83.33	79.01	77.82	73.73	84.84
LOI		15.17	17.20	14.16	13.77	16.36	15.12	14.45	13.01	13.32	12.96	15.09	17.58	18.26	20.43	14.76
Al_2O_3/SiO_2		0.058	0.038	0.057	0.052	0.020	0.023	0.038	0.027	0.047	0.030	0.051	0.034	0.046	0.042	0.057
MgO/SiO_2		0.861	0.856	0.893	0.851	0.937	0.901	0.874	0.880	0.877	0.857	0.907	0.871	0.898	0.890	0.974
Fe(III)/ ∑Fe[a]		0.787	0.792	0.797	0.803	0.931	0.827	0.805	0.648	0.597	0.607	0.611	0.859	0.922	0.906	0.639
2 SD		0.091	0.101	0.060	0.085	0.140	0.088	0.094	0.065	0.090	0.113	0.088	0.116	0.114	0.174	0.058
Magnetite[b]	wt%	0.50	1.34	1.73	0.45	0.90	0.64	0.53	1.42	0.41	0.92	0.73	0.48	0.29	0.29	0.34
As	mg kg^{-1}	9	10	8	7	9	10	8	8	7	6	6	11	14	15	7
Ba		<30	<30	<30	<30	76	34	<30	<30	<30	<30	<30	439	<30	54	<30
Co		100	105	114	105	389	96	72	131	115	121	116	189	81	155	142
Cr		3,825	2,726	3,305	2,990	2,670	2,159	2,548	2,932	3,118	2,610	3,236	2,281	4,344	3,229	2,648
Cu		29.9	13.6	20.1	23.1	14.8	15.2	13.8	10.5	28.2	25.4	22.5	26.5	15.8	29.3	29.8
Ga		<3	<3	<3	<3	<3	<3	<3	<3	<3	<3	<3	<3	<3	<3	<3
Mo		2	20	<2	2	4	<2	<2	2	2	<2	<2	3	<2	7	5
Nb		<2	<2	<2	<2	<2	<2	<2	<2	<2	<2	<2	<2	<2	<2	<2
Ni		2,557	2,245	2,429	2,409	2,200	2078	2,331	2,821	2,478	2,742	2,564	2,326	3,482	3,278	3,004
Pb		<4	<4	<4	<4	<4	<4	<4	<4	<4	<4	<4	<4	<4	<4	<4
Rb		19	18	15	13	18	14	16	13	14	14	13	17	19	20	15
Sr		34	39	29	26	38	34	28	11	13	8	23	109	62	83	6
Th		7	8	10	6	11	6	9	7	5	6	6	11	9	13	6
U		<3	<3	<3	<3	<3	<3	<3	<3	<3	<3	<3	<3	<3	<3	<3
V		69	52	53	52	38	30	41	35	51	40	56	43	69	75	60
Y		<2	<2	<2	<2	<2	<2	<2	<2	<2	<2	<2	<2	<2	<2	<2
Zn		31	26	28	28	32	19	23	26	26	18	24	28	78	111	26
Zr		9	7	9	9	7	5	8	6	8	7	9	8	10	10	7

[a]*From Mössbauer spectroscopy.*
[b]*From magnetometry.*

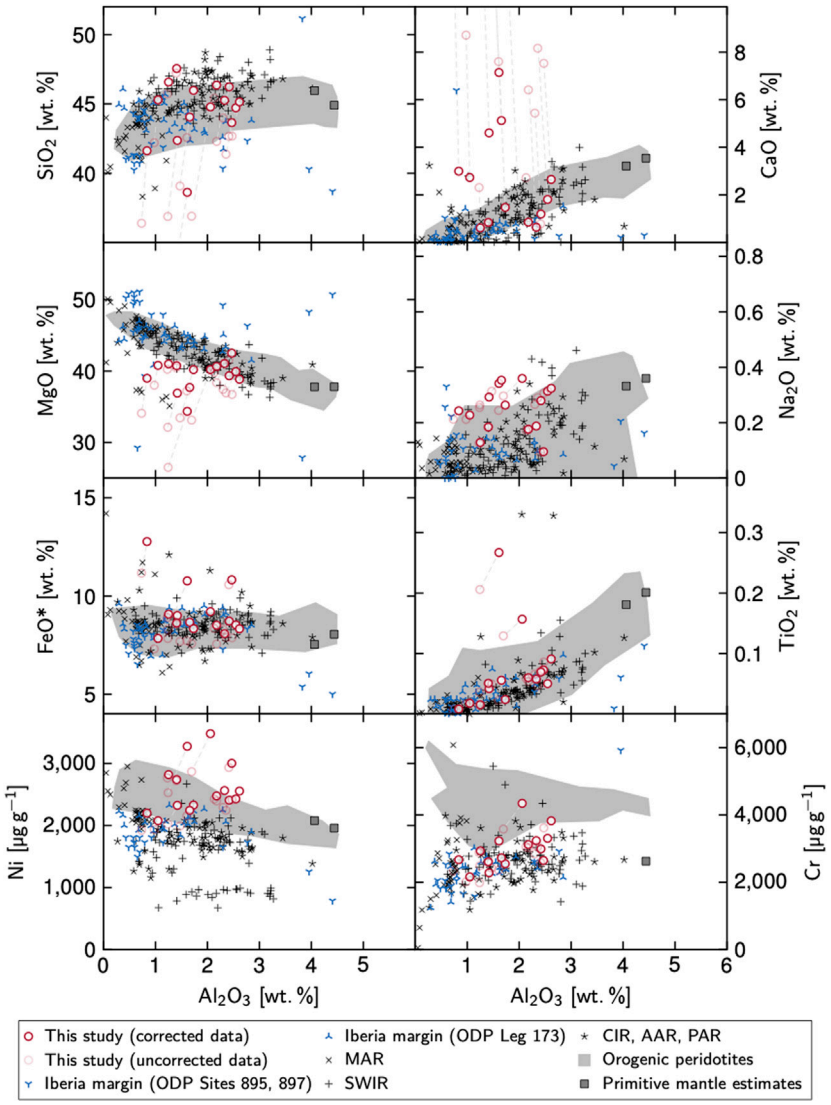

FIGURE 3 | Bulk rock geochemical compositions of the Hole 637A serpentinites. Shown are data before and after the correction for late-stage $CaCO_3$ metasomatism; dashed lines connect corrected (red circles) with uncorrected compositions (transparent red circles). For comparison, bulk compositions from other Iberia margin rocks (Seifert and Brunotte, 1996; Hébert et al., 2001), MOR sites (Seyler et al., 2003; Kelemen et al., 2004; Niu, 2004; Godard et al., 2008; Jöns et al., 2010), tectonically emplaced "orogenic" peridotites (Bodinier and Godard, 2014), and of primitive mantle estimates (Hofmann, 1988; McDonough and Sun, 1995) are shown. Abbreviations: AAR, American–Antarctic Ridge; CIR, Central Indian Ridge; MAR, Mid-Atlantic Ridge; PAR, Pacific–Antarctic Ridge; SWIR, Southwest Indian Ridge.

(**Supplementary Figures S3A,B**). Temperature cycling of the latter sample points to a chemical composition close to stoichiometric magnetite and hence strengthens the above interpretation. Results of sample 25R-4, by contrast, suggest significant partial oxidation of magnetite. Further details can be found in the caption of **Supplementary Figure S3**.

Bulk magnetization analyses revealed magnetite contents from 0.29 to 1.73 wt%, with a median of 0.53 wt% (**Table 2**). The least modified samples hold a median of 0.83 wt% of magnetite whereas contents in oxidized and metasomatized samples are 0.53 and 0.41 wt%, respectively. No clear relation between magnetite content and coring depth has been observed.

Mineral Chemistry

Clinopyroxene has X_{Mg} values typically in the range of 0.92–0.94, Al_2O_3 contents ranging from 3.3–6.2 wt%, TiO_2 between 0.1 and 0.4 wt%, and Na_2O contents between 0.58 and 1.09 wt%. Orthopyroxene has slightly lower X_{Mg} values (0.91–0.92), and typically contains 3.5–5.2 wt% Al_2O_3, <1 wt% CaO (except where close to clinopyroxene exsolution lamellae), and <0.1 wt% Na_2O. Primary spinel has X_{Cr} = Cr/(Cr + Al)

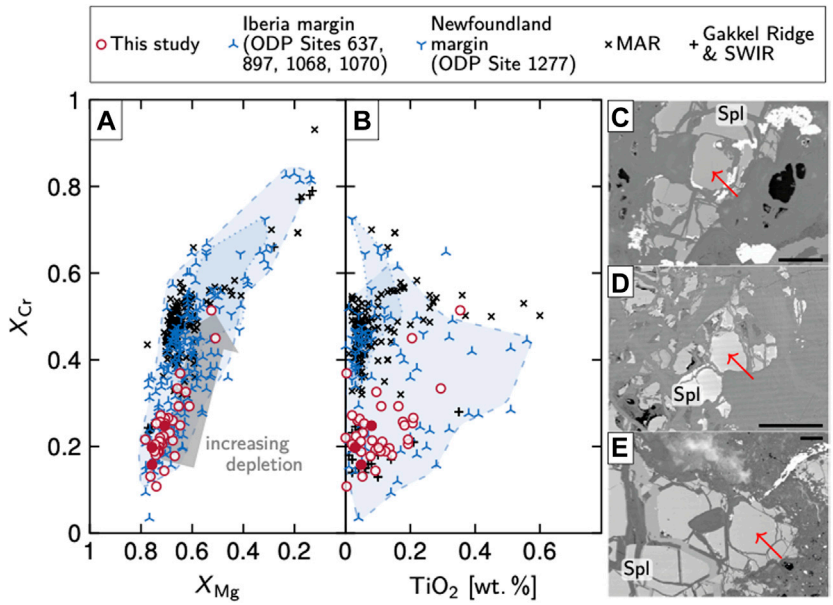

FIGURE 4 | X_{Mg} vs. X_{Cr} **(A)** and TiO_2 vs. X_{Cr} **(B)** characteristics of spinel in Hole 637A rocks. Spinels are Mg- and Al-rich and generally indicate little melt depletion. The three solid red circles correspond to the spinel grains in BSE images **(C)** to **(E)** (samples 27R-1, 107–110 cm, 27R-2, 65–68 cm, and 28R-1, respectively; arrows show analysis locations; scale bars are 100 μm). Spinel compositions from other sites at the Iberia–Newfoundland conjugate margin (areas with dashed and dotted outlines, respectively) and from the slow-spreading MAR and the ultraslow-spreading Gakkel and Southwest Indian Ridges are shown for comparison. Data are from Evans and Girardeau (1988), Cornen et al. (1996; analyses of spinel cores only), Seifert and Brunotte (1996), Abe (2001), Hebert et al. (2001; digitized with WebPlotDigitizer, https://automeris.io/WebPlotDigitizer/), Hellebrand et al. (2002), Chazot et al. (2005); Müntener and Manatschal (2006), Seyler et al. (2007), Moll et al. (2007), Tamura et al. (2008), Vils et al. (2008), Silantyev et al. (2011), Kodolányi et al. (2012) and Dessimoulie et al. (2020). All values are cations per formula unit, calculated on the basis of four O with all Fe treated as ferrous. Abbreviations: MAR, Mid-Atlantic Ridge; Spl, spinel; SWIR, Southwest Indian Ridge.

values usually within 0.13 and 0.45 and X_{Mg} of 0.52–0.76 (**Figure 4A**). The cores of large grains are usually unzoned; in a few instances, as for example when chlorite occurs close to spinel, slight increases in Cr and Fe toward the rims were observed. Contents of TiO_2 in spinel are mostly <0.15 wt% but can reach up to 0.25 wt% (**Figure 4B**).

Secondary phases show variable compositions. The bulk of these phases can be identified as serpentine, with median X_{Mg} of 0.93 ± 0.05 (1 SD; n = 256; **Figure 5A**). Elevated Fe contents in a number of analyses (X_{Mg} as low as 0.43) point toward a cronstedtite component in serpentine. The Fe-rich serpentine occurs either in the centers of mesh textures (**Figure 2F** and **Supplementary Figures S4B–D**) or as porous, void-filling precipitates (**Figure 2H**). We could, however, not record clear cronstedtite spectra during reconnaissance micro-Raman analysis, presumably due to an overprint by lizardite (**Supplementary Figure S5**). The serpentine can further contain high concentrations of Al (up to ~1.5 cations per formula unit), which suggest solid solutions with the Al-rich serpentine-group mineral amesite (**Figure 5B**). We also observed a distinct trend toward Si/(Mg + Fe) ratios higher than that of serpentine, indicative of talc occurring intergrown with serpentine to variable degrees (**Figure 5A** and **Supplementary Figure S4A**). Some of these analyses with elevated Si/(Mg + Fe) exhibit high Na_2O contents, which imply intergrowth of serpentine with the smectite-group mineral stevensite (**Figure 5C**; cf. Sakharov et al., 2004; Obeso and Kelemen, 2020). These serpentine–stevensite–talc mixtures are restricted to the void-filling precipitates (**Supplementary Figures S4B–D**). Microprobe data do not imply the presence of brucite in any sample.

Amphibole can be classified as hornblende to tremolite. It has X_{Mg} of 0.91–0.96, variable amounts of Al_2O_3 (0.1–15.4 wt%) and TiO_2 (<0.1–3.2 wt%), between 10.9 and 13.5 wt% CaO, and 0.1 to 2.9 wt% Na_2O. Values of X_{Mg} anticorrelate whereas those of Al_2O_3 correlate with Na_2O contents. High TiO_2 correlates with high Al_2O_3.

Mineral compositional data are reported in **Supplementary Table S2**.

Geochemical Modeling Results

We applied thermodynamic calculations to track the amounts of H_2 that are being produced during serpentinization at magma-poor margins such as the West Iberia margin. **Figures 6A–D** summarize results for seawater–basement reactions at an OCT, based on the composition of sample 25R-2, 62–65 cm, demonstrating intermediate composition between those of SCLM and strongly depleted harzburgitic/dunitic rocks commonly found at MORs (cf. **Figure 2**; see also *Degree of Melt Depletion at Hole 637A*). Over most of the investigated

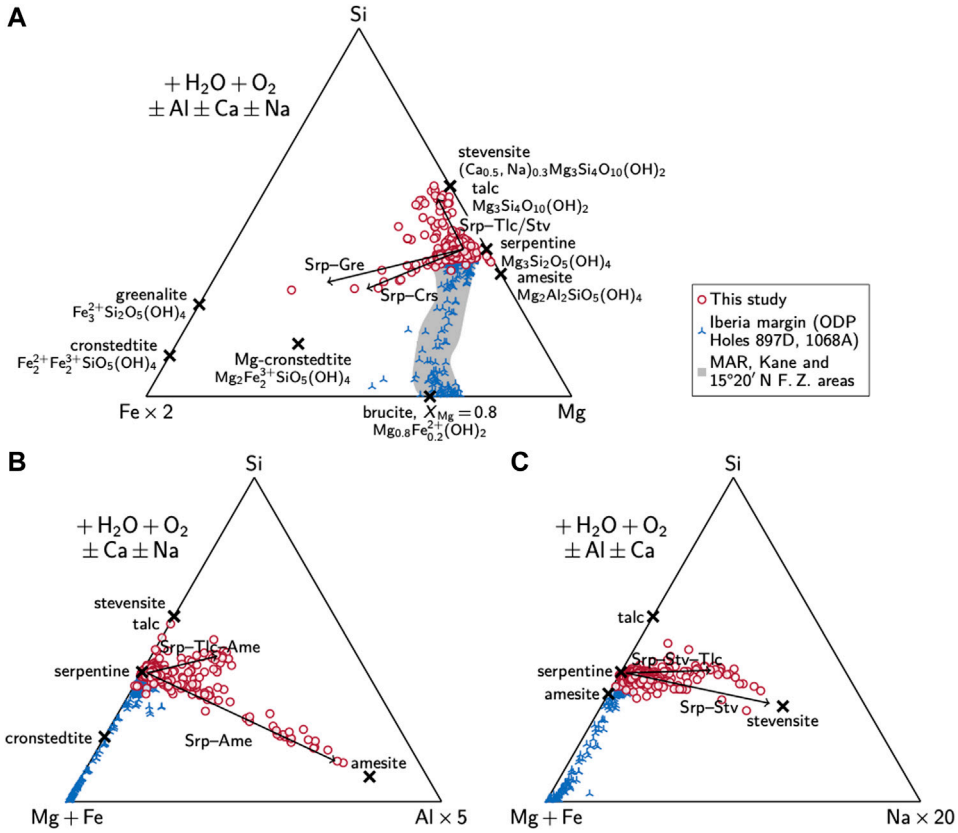

FIGURE 5 | Si–Fe–Mg–Al–Na systematics of secondary phases in Hole 637A samples **(A)** The bulk of the analyses suggests high-X_{Mg} serpentine; intergrowth with stevensite and/or talc, serpentine–cronstedtite solid solutions, and mixtures thereof may explain analyses richer in Si and/or Fe. There are no indications of intergrowth with brucite, as is common in ODP Holes 897D and 1068A (Klein et al., 2014) and at the MAR (data from Moll et al., 2007; Klein et al., 2009; Andreani et al., 2013 are shown for comparison) **(B)** Aluminum contents imply serpentine–amesite mixtures as well as intergrowth of serpentine, amesite, and stevensite/talc **(C)** Varying contents of Na imply the presence of stevensite and talc. All values are cations per formula unit, calculated on the basis of seven O. Abbreviations: Ame, amesite; Brc, brucite; Crs, cronstedtite; Gre, greenalite; Srp, serpentine; Stv, stevensite; Tlc, talc.

temperature range, the equilibrium mineral assemblage (**Figure 6A**) consists of serpentine, amesite, and clinopyroxene. Olivine and magnetite are predicted to be stable only at/above 400°C. Below ~150°C, trace amounts of brucite are predicted.

The X_{Mg} of serpentine plots at ~0.89 independent of temperature, with a fraction of ferric Fe in serpentine of ~0.2 at 380–150°C that decreases toward ~0.1 at 25°C once brucite has joined the assemblage (**Figure 6B**). Serpentine hence hosts up to 0.29 moles Fe(III); the proportion of ferric Fe contributed by magnetite is minor (**Figure 6C**). As a consequence, the predicted amounts of H_2(aq) per kg rock are ~150 mmol at ~380–150°C but <100 mmol toward seawater temperatures (**Figure 6D**).

Figures 6E–H demonstrate the consequences of fluid–SCLM interactions, based on the undepleted mantle composition by Salters and Stracke (2004). We chose this composition as a counterpart to the strongly depleted compositions found at MORs to demonstrate the consequences of high modal pyroxene contents for serpentinization. The predicted equilibrium assemblage yields slightly higher amounts of magnetite and brucite, which are stable over larger temperature ranges (**Figure 6E**). The X_{Mg} of brucite drops from 0.83 at ~220°C to 0.59 at 25°C (**Figure 6F**). The fraction of ferric Fe is highest at ~380–220°C where both serpentine and magnetite are stable, with Fe(III)/∑Fe of 0.32, but decrease as brucite becomes stable and progressively richer in Fe (**Figure 6F**). Up to 0.37 moles Fe(III) are produced by the co-occurrence of serpentine and magnetite; once magnetite is no longer part of the equilibrium assemblage, this number drops to <0.3 moles and further decreases with decreasing temperature (**Figure 6G**). The predicted amount of H_2(aq) follows that of ferric Fe (**Figure 6H**).

Results from model runs at w/r ratios of 10 as well as those in which the formation of garnet is allowed are shown in **Supplementary Figures S6, S7**, respectively.

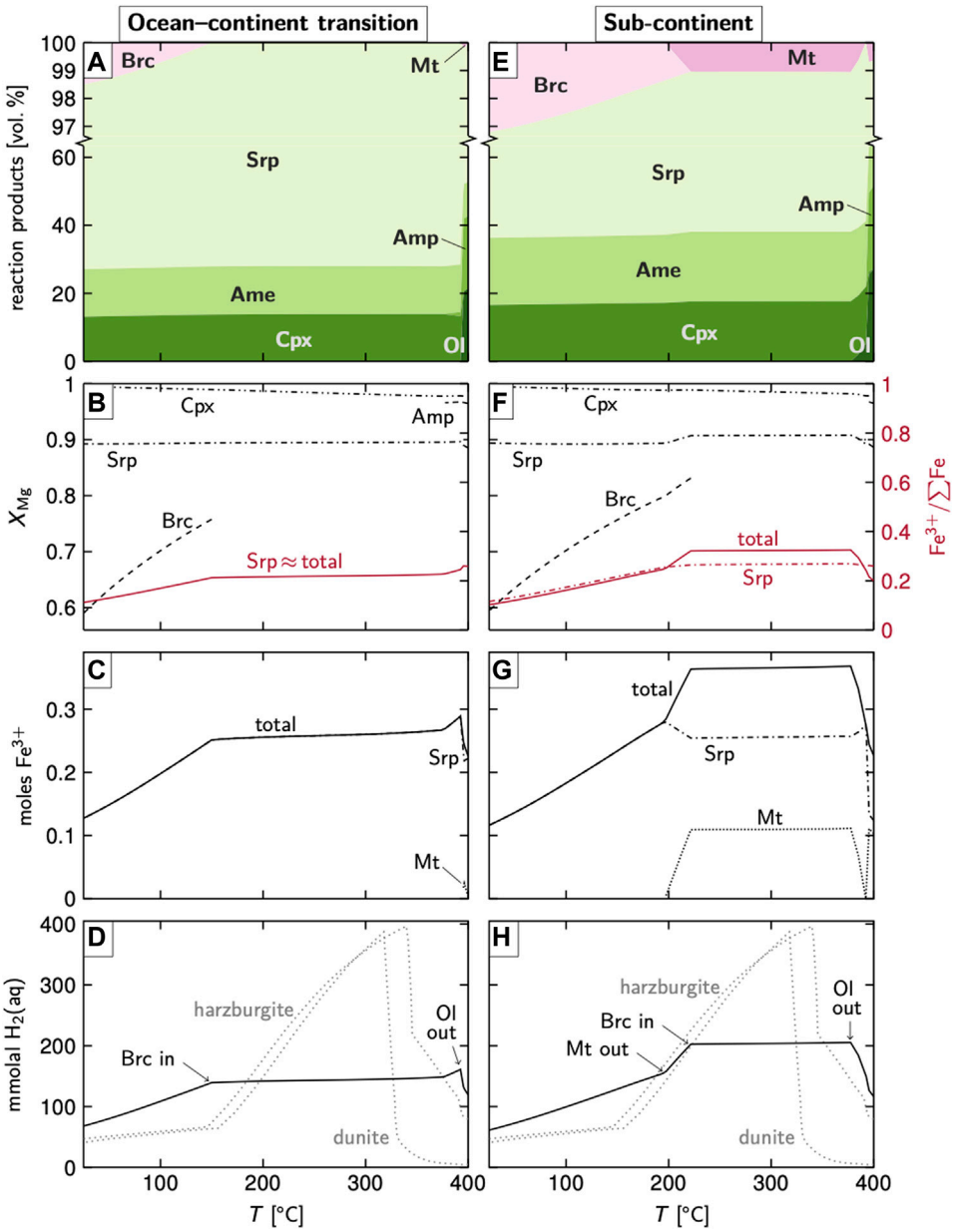

FIGURE 6 | Thermodynamic modeling results using bulk compositions representative of rocks from proximal domains of an OCT **(A–D)** and the SCLM **(E–H)** at w/r = 1. The formation of garnet is suppressed in these runs. Plots **(A)** and **(E)** show predicted equilibrium mineral assemblages **(B)** and **(F)** show Fe–Mg relations of the stable phases and the oxidation states of Fe **(C)** and **(G)** give the amounts of Fe(III) per kg rock, and **(D)** and **(H)** depict the respective amounts of H_2(aq) produced from the oxidation of Fe. Amounts of H_2(aq) predicted for the hydration of harzburgitic and dunitic rocks are shown for comparison (Klein et al., 2009). Abbreviations: Ame, amesite; Amp, amphibole; Brc, brucite; Cpx, clinopyroxene; Mt, magnetite; Ol, olivine; Srp, serpentine.

DISCUSSION

Hydrothermal Alteration at Hole 637A

Initial Pervasive Serpentinization

The serpentinites investigated here show evidence for a high-temperature strain and metamorphism history, as evidenced by microtextures indicative of ductile deformation and the occasional presence of amphibole, respectively (e.g., **Figure 2B**; cf. Agrinier et al., 1988; Kimball and Evans, 1988). Subsequent to these, extensive fluid–rock interactions took place at lower temperatures. Early serpentinization of the samples is distinguishable from prolonged interaction with seawater on the basis of petrographic observations and bulk rock and mineral chemical data.

The initial stage of serpentinization was mostly pervasive. Whereas primary spinel is preserved in all samples, olivine is completely altered to serpentine minerals and trace amounts of Fe oxides, often in pseudomorphic mesh textures. Microtextures

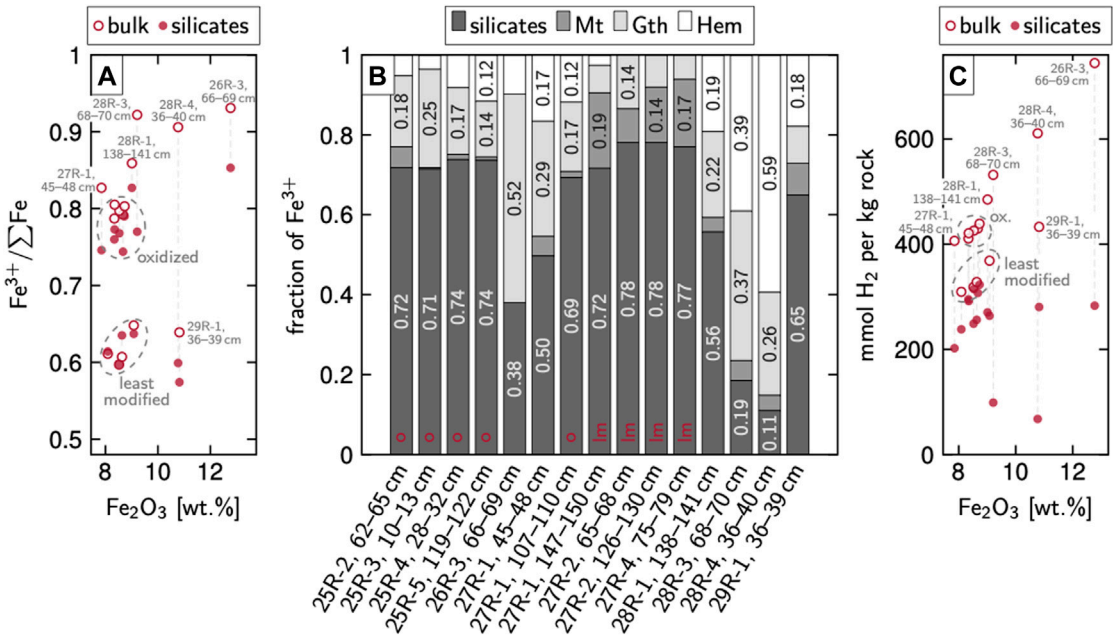

FIGURE 7 | Contents and distribution of Fe(III) in Hole 637A serpentinites and inferred H_2 production **(A)** Total Fe_2O_3 from bulk geochemistry vs. Fe(III)/∑Fe of bulk rock and silicates from Mössbauer spectroscopy. Most of the ferric Fe in silicates is likely hosted by serpentine. Dashed lines connect values of individual samples **(B)** Distribution of Fe(III) within the individual samples. In most samples, silicates comprise about 70% whereas magnetite hosts only minor amounts of ferric Fe. Labels 'o' and 'lm' refer to oxidized and least modified, respectively **(C)** Total Fe_2O_3 vs. amounts of H_2 produced during the oxidation of the samples, as calculated on the assumption that all Fe has initially been ferrous and was oxidized by H_2O during the fluid–rock interactions. Abbreviations: Gth, goethite; Hem, hematite; Mt, magnetite.

indicative of deformation at higher temperatures are statically replaced by serpentine. Higher X_{Mg} in serpentine (median = 0.93) relative to that of its precursor olivine (ranging from 0.894 to 0.906; Kimball and Evans, 1988) implies that Fe has been redistributed during alteration. We thereby exclude that large amounts of Fe have been incorporated into brucite, since the breakdown of pyroxene likely caused high SiO_2 activities ($aSiO_2$) during serpentinization that prevented brucite formation in the first place (cf. Frost and Beard, 2007). Instead, it is likely that most of the serpentinization occurred *via* the reaction $Mg_2SiO_4 + 2\ SiO_2 + 4\ H_2O = 2\ Mg_3Si_2O_5(OH)_4$, with SiO_2 derived from the dissolution of pyroxene through the reaction $3\ MgSiO_3 + 2\ H_2O = Mg_3Si_2O_5(OH)_4 + SiO_2$. In line with this conclusion are pyroxene grains that are in most cases strongly reacted (cf. **Figure 2**), the lack of brucite in any of our samples (**Figure 5**), and thermodynamic calculations predicting only trace amounts of brucite for the reaction of a representative sample with seawater-derived fluid (**Figure 6**). Hence we do not interpret the putative loss of bulk MgO in some of our samples (**Figure 3C**) as the dissolution of brucite during prolonged seawater interaction (e.g., Snow and Dick, 1995; Klein et al., 2020), but as a metasomatism-related dilutional effect (it is the samples with high CaO that appear particularly MgO-poor). Thus, instead of being partitioned into brucite, we infer that most Fe has likely been partitioned into serpentine and/or scarce magnetite, the latter of which occurs evenly distributed in some but very heterogeneously in other samples.

Initial serpentinization resulted in Fe(III)/∑Fe of ~0.6 (least modified samples in **Figure 7A**), very similar to the Fe oxidation state in serpentinites from the Mid-Atlantic Ridge (MAR; Andreani et al., 2013; Klein et al., 2014). Serpentine thereby contains more than 3/4 and thus the bulk of the ferric Fe and magnetite holds another ~15–20% (**Figure 7B**). The Fe-rich serpentine mesh centers presumably host a large portion of the Fe(III) but in samples without such mesh centers, Fe(III) must be present elsewhere—bulk magnetization analyses suggest a median of 0.83 wt% magnetite for the least modified samples (**Table 2**). However, this number may serve as a minimum estimate for magnetite production during initial serpentinization since minor amounts of goethite and hematite may have formed after magnetite and hence, initial magnetite contents may have been slightly higher. This alteration likely also lowered the measured relative fraction of Fe(III) in serpentine (**Figure 7B**). Nevertheless, conclude that generally little magnetite has been produced during initial serpentinization. Our reaction path models match this assumption as they do not predict any magnetite in the equilibrium assemblage over most of the temperature range (**Figure 6A**). This is at least true for the case of a composition representing low to intermediate stages of melt depletion, as was used in our models. But the peridotites recovered from Hole 637A are compositionally very diverse, ranging from lherzolitic to dunitic (Boillot et al., 1987) and it is hence likely that other lithologies have influenced the fluid–rock interactions. For instance, ~1 wt% of magnetite would

be produced during the hydration of undepleted lithologies (**Figure 6E**), and even higher portions for strongly depleted rocks such as harzburgites or dunites (Klein et al., 2009; McCollom and Bach, 2009). Furthermore, aside from the composition of the protolith, the alteration temperature and the extent of serpentinization are factors that to a major degree influence the amounts of magnetite being produced. Andreani et al. (2013) and Klein et al. (2014) demonstrated that magnetite contents non-linearly correlate with increases in temperature and the serpentinization extent. All peridotites recovered from Hole 637A as well as from nearby holes drilled during ODP Legs 149 and 173 are extensively serpentinized and yet hold little magnetite (Boillot et al., 1987; Sawyer et al., 1994; Whitmarsh et al., 1998), indicating low hydration temperatures. This general interpretation has been validated by results from O stable isotopes, which consistently imply serpentinization temperatures at the West Iberia margin of below 200°C (Agrinier et al., 1988; Agrinier et al., 1996; Schwarzenbach et al., 2013; Klein et al., 2014). Altogether, the median magnetite content of our least modified samples (0.83%) falls markedly below contents typical for MORs (4–6%; e.g., Klein et al., 2014).

Instead of having been partitioned into brucite and/or magnetite, Fe was incorporated into serpentine as indicated by our mineral chemical data (**Figure 5**). About 16% of the total analyses ($n = 256$) exhibit $X_{Mg} < 0.9$ and the median X_{Mg} of the lowest 10% is 0.83. In particular, the centers of serpentine mesh textures can be enriched in Fe, whereas mesh rims and intergranular serpentine usually represent "typical" Mg-rich serpentine (**Figure 2F** and **Supplementary Figures S4B–D**). Such serpentine with higher Fe contents in mesh centers has previously been described by Kimball and Evans (1988). Our data imply a high cronstedtite component, which is further discussed in *Formation of Cronstedtite and H_2 During Initial Serpentinization*.

Ortho- and clinopyroxene are mostly altered to bastite serpentine but domains of unserpentinized pyroxene are locally preserved in most samples. This can either suggest that the alteration conditions were favorable for the (meta-)stable preservation of pyroxene or that pyroxene reacted at considerably slower rates in comparison to olivine. The relative rates of pyroxene and olivine reaction are a matter of recent debate (see, e.g., discussion in McCollom et al., 2020). Thermodynamic modeling results suggest that clinopyroxene is stable throughout the considered temperature range at w/r ratios close to unity (**Figure 6**). Somewhat contrastingly, petrographic observations in some cases revealed clinopyroxene that is partially serpentinized (**Figure 2C**). These observations are more in agreement with model runs at higher w/r ratios, at which pyroxene is no longer part of the equilibrium assemblage (**Supplementary Figure S6A**). Prolonged late-stage interaction with seawater (see below) is also not accounted for by the models but could explain local clinopyroxene serpentinization. Orthopyroxene is not predicted to be stable in any model run, which fits with petrographic observations revealing that orthopyroxene is in most cases strongly reacted.

Oxidation and Mass Transfer During Prolonged Fluid–Rock Interactions

The interaction with seawater did not cease subsequent to the initial serpentinization but instead continued and led to further mineralogical and geochemical modifications. Calcite is very common and occurs in veins and void space (**Figures 2B,D,I**), the latter of which probably represent the centers of former olivine grains. Calcite abundance is reflected in the bulk geochemistry, which can exhibit up to 21.5 wt% CaO and 17.1 wt% CO_2 (uncorrected data, **Supplementary Table S1**). Both CaO and CO_2 were added to the rocks by cold, circulating seawater as was proposed earlier for West Iberia margin drill sites (Evans and Baltuck, 1988; Gibson et al., 1996). Euhedral Fe oxides that match the stoichiometry of magnetite are present within many calcite veins (**Figure 2I**; see also Evans and Baltuck, 1988), suggesting either that Fe was added to the seafloor together with the calcite or that Fe was released during the dissolution of Fe-containing minerals and was subsequently re-precipitated in the present form. The former may be true for samples in which bulk Fe_2O_3 is increased relative to "typical" serpentinite (**Figures 3**, **7**). Bulk Fe_2O_3 concentrations of most samples do not, however, display noticeable enrichments and thus support the latter possibility. The common observation of dissolved mesh center argues for the dissolution of olivine and/or serpentine during late fluid–rock interactions. Calcite that occurs in mesh centers which are comparable in size and location to the olivine or serpentine cores found in other samples has previously been described from Hole 637A (Kimball and Evans, 1988). Similar conclusions have been drawn based on observations in weathered peridotites from the MAR, in which open voids in the centers of mesh textures host Fe hydroxides that apparently precipitated from void-filling fluids after the dissolution of brucite and/or olivine (Jöns et al., 2017). These rocks also contain abundant carbonate that, besides being present in veins, fills the voids alongside Fe hydroxide.

The Site 637 samples further show evidence for the formation of a late serpentine generation (**Figure 2H**) with highly porous serpentine that frequently exhibits X_{Mg} of <0.9 (**Supplementary Figure S4B**) and elevated Na contents. Microtextures suggest precipitation in void space and the mineral chemistry implies intergrowth of serpentine with a strong cronstedtite-component, stevensite, and talc (**Figure 5**). It presumably is this cronstedtite-rich serpentine that accounts for the shift of the fraction of Fe(III) in serpentine from ~0.6 in the least modified to ~0.75 in oxidized samples (**Figure 7A**). This shift can be observed in 1/3 of our samples and we suggest that this is related to heterogeneities in porosity and permeability between the individual portions of rock that led to different degrees of seawater influx and reaction. Indeed, the precipitation of carbonate may even clog further inflow of seawater and hence reduce the permeability (cf. Jöns et al., 2017). The bulk Fe(III)/∑Fe of these samples has increased to ~0.8 (**Figure 7A**) and highlights the general oxidation of the seafloor caused by the prolonged interaction with seawater. It is within these samples from the shallowest core sections that goethite and hematite appear to have replaced most of the magnetite, similar to what has been described for Site 1068 (Beard and Hopkinson, 2000). These phases now hold, on

average, more than 20% of the total Fe(III). The presence of maghemite is also likely (cf. Zhao, 2001; Oufi et al., 2002) but it cannot be confirmed with the analytical techniques used in this study.

Overall, these observations document the prolonged low-temperature interaction with fluids at/close to the seafloor. This interpretation is supported by the presence of calcite that precipitated at or close to ambient deep-sea temperatures (Agrinier et al., 1988; Evans and Baltuck, 1988). Similarly, serpentine may at least in parts have formed at temperatures ≫100°C, as implied by serpentine O stable isotope values between ~9 and 12‰ (relative to SMOW; Agrinier et al., 1988). We think that this is the case for the observed porous late serpentine generation, most of which we observed in samples from the shallow core sections. For these sections, Evans and Baltuck (1988) suggest highest water/rock ratios during alteration. The intergrowth of stevensite and talc, however, may also suggest that the serpentinites interacted with sedimentary pore waters instead of pure seawater (cf. Barnes and Sharp, 2006).

In the metasomatized samples, high abundances of goethite and hematite are remarkable (**Figure 7B**). These samples contain high amounts of calcite (whole rock data show consistent enrichments in $CaCO_3$), host Fe oxides and oxyhydroxides, and in some cases serpentine with variable X_{Mg}. Microtextures are in many cases indicative of mineral growth in equilibrium with a fluid. Oxides rich in Mn, Co., and/or Ti are present in trace amounts. It appears likely that the former fractures—now filled with vein precipitates—provided pathways for enhanced seawater flow through these portions of the seafloor. This seawater interaction also led to the addition of Fe in some of the metasomatized samples, as previously proposed by Gibson et al. (1996), and in all samples to the oxidation of most of the Fe that is not contained in serpentine. The portions of ferric Fe in serpentine, however, appear unchanged as they are within or close to the range of the least modified or oxidized samples.

H_2 Production During Seawater–Basement Interactions at Hole 637A

Formation of Cronstedtite and H_2 During Initial Serpentinization

During serpentinization, H_2 is produced during the oxidation of ferrous to ferric Fe. Ferric Fe is incorporated in magnetite, $Fe^{2+}Fe_2^{3+}O_4$, and/or the serpentine-group endmember cronstedtite, $(Mg,Fe^{2+})_2Fe_2^{3+}SiO_5(OH)_4$. In the samples investigated here, the amount of ferric Fe in serpentine and hence H_2 production associated with the formation of cronstedtite outweighs that in/related to magnetite (**Figure 7B**).

Cronstedtite substitution in serpentine describes the partial exchange of Fe^{2+} and/or Mg with Fe^{3+}, which is accompanied by a $Fe_2^{3+}(Fe^{2+}Si)_{-1}$ exchange to maintain charge balance (e.g., O'Hanley and Dyar, 1993). If it went to completion, the substitution would result in the endmembers Fe-cronstedtite, $Fe_2^{2+}Fe_2^{3+}SiO_5(OH)_4$, or Mg-cronstedtite, $Mg_2Fe_2^{3+}SiO_5(OH)_4$, or mixtures thereof.

The presence of cronstedtite by itself is not unusual for marine serpentinites. It can be approximated by analyzing serpentinite Fe(III)/∑Fe; generally, between 50 and 60% of the Fe in MOR and passive margin serpentinites are ferric, even in ones containing little magnetite (Mayhew and Ellison, 2020). But X_{Mg} values for serpentine in these rocks rarely fall below 0.9 and the total contents of Fe_2O_3 in serpentinites are usually below 7–8 wt% (cf. Mayhew and Ellison, 2020).

Most of the serpentine analyzed here plot in the typical X_{Mg} range of 0.9–0.95 (median = 0.93) but several samples also exhibit serpentine with X_{Mg} values well below 0.9 in mesh centers and strongly suggest a pronounced cronstedtite component (**Figures 2F**, **5A**). The stability of cronstedtite is primarily dependent on $aSiO_2$ and H_2 fugacity during serpentinization (e.g., Zolotov, 2014; Tutolo et al., 2020). Serpentine with minor cronstedtite fractions can be formed under rather variable conditions, but higher cronstedtite components require increasing $aSiO_2$ (**Figure 8**). As discussed above, such elevated-$aSiO_2$ conditions likely prevailed during the initial serpentinization of the lherzolitic rocks as well as during their late interaction with (sediment-derived) fluids.

Based on our Mössbauer data, 60–65% of the Fe in serpentine of the least modified samples is ferric (**Figure 7A**). Serpentine of such composition can be explained by mixing of serpentine–greenalite with Mg-cronstedtite (**Figure 9**). One kg of pure serpentine with Fe(III)/∑Fe of 0.65 and X_{Mg} of 0.95 would produce about 150–170 mmol H_2, assuming that H_2O was the only oxidant. This hypothetical value is in the same order of magnitude as our modeling results (~120–160 mmol H_2 per kg rock at 120–200°C; **Figures 6D,H**) and previous thermodynamic models for lherzolitic compositions (Klein et al., 2013). By comparison, ~430 mmol H_2 would be produced per kg serpentine with X_{Mg} = 0.88, as observed in mesh centers (**Figure 9**). Assuming that such serpentine accounts for 1/5 to 1/4 of the entire serpentine at the West Iberia margin, H_2 yields of ~215–230 mmol H_2 appear realistic per kg serpentine—which is almost twice as much as if such Fe-rich serpentine were not present. Hydrogen fluxes calculated based on our Mössbauer data are even higher (up to 260 mmol H_2 per kg serpentine; **Figure 7C**), but these likely are slight overestimations since some of the oxidation may have been caused by oxidizing agents other than H_2O (e.g., SO_4^{2-}).

The scarcity or absence of magnetite in the least modified samples (median = 0.83 wt%; **Table 2**) hence does not signify a lack of oxidation or that no hydrolysis has taken place. However, magnetite formation in these rocks has even increased the fluxes of H_2 up to >300 mmol per kg bulk rock (**Figures 7B,C**).

The bulk of the pervasive serpentinization likely took place during seawater seepage into the seafloor at w/r ratios close to unity. In addition, however, tectonic activity likely provided fluid pathways at/close to which each rock unit reacted with larger amounts of fluid. Our thermodynamic estimates revealed mineral assemblages dominated by serpentine for both undepleted to weakly-depleted compositions at w/r ratios of 10 (**Supplementary Figure S6**). Amounts of Fe(III) are <0.4 mole per kg rock in both cases, translating to 50–120 mmol H_2(aq) produced at >250°C but ≪50 mmol at lower temperatures.

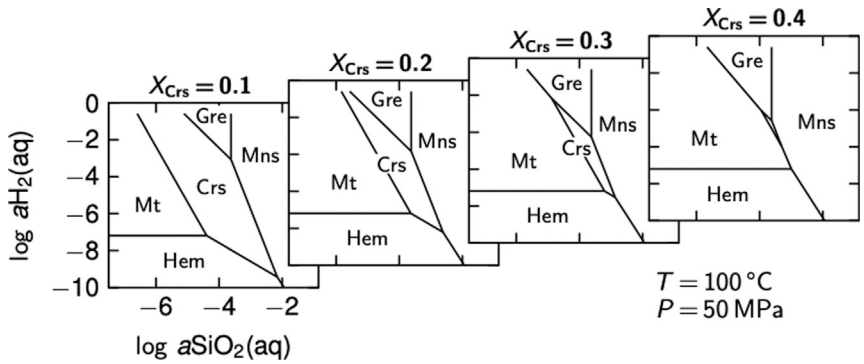

FIGURE 8 | Stability of Mg-serpentine–cronstedtite mixtures with increasing fraction of cronstedtite, X_{Crs} (from left to right). Pure cronstedtite is not stable at the 500 MPa and 100°C, but serpentine with low cronstedtite components may be stable at silica activities that are intermediate between those of magnetite and greenalite. It may hence form under quite variable conditions, which are conceivable for diverse settings and lithologies including harzburgite and dunite at MORs. Serpentine with cronstedtite fractions as low as 0.1 require $aSiO_2$ higher than that of the serpentine–brucite buffer ($10^{-6.8}$ at 500 MPa and 100°C, with X_{Mg} of serpentine = 0.95 and X_{Mg} of brucite = 0.8), which may restrict its presence to lherzolitic rocks. The diagrams were constructed using Geochemist's Workbench® and data from SUPCRT92 and Wolery and Jove-Colon (2004) for cronstedtite. Ideal mixing with $a_{Crs} = X_{Crs}^{2.5}$ was assumed. Abbreviations: Crs, cronstedtite; Gre, greenalite; Hem, hematite; Mns, minnesotaite; Mt, magnetite.

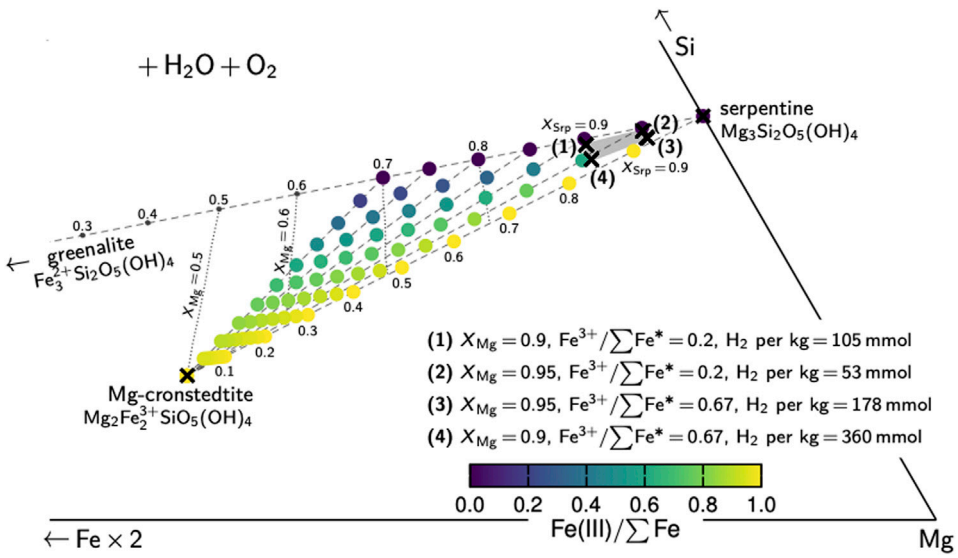

FIGURE 9 | Hypothetical mixing between different serpentine-group endmember compositions. Dashed lines represent mixing between serpentine, greenalite, and Mg-cronstedtite, and between serpentine–greenalite mixtures and cronstedtite, with decreasing serpentine fractions (X_{Srp}). Dotted lines are resulting X_{Mg} compositions and colored circles represent resulting Fe(III)/∑Fe compositions. Serpentine from natural settings mostly varies between X_{Mg} of 0.9 and 0.95 and Fe(III)/∑Fe of 0.2–0.65 (gray shaded field), which can be explained by mixing of $Srp_{0.9–0.95}Gre_{0.05–0.1}$ with Mg-cronstedtite.

Late-Stage Serpentinite Oxidation and H_2 Production

Seawater–serpentinite reaction after their exposure to the seafloor caused additional H_2 fluxes, related to the formation of Fe(III)-serpentine–stevensite–talc mixtures and the formation and transformation of Fe oxides and/or hydroxides. The former was favored by increased $aSiO_2$ (cf. **Figure 8**) and resulted in the release of another ~50 mmol H_2 per kg rock (**Figure 7C**). The latter was particularly pronounced in the shallow, strongly oxidized core sections of Hole 637A, in which much of the magnetite has turned into hematite and goethite (**Figures 7A,B**). This modification likely took place in two steps, namely the oxidation of magnetite to hematite, 4 Fe_3O_4 + H_2O = 6 Fe_2O_3 + H_2(aq), and the formation of goethite at the expense of hematite, $Fe_2O_3 + H_2O$ = 2 FeO(OH) (cf. Klein et al., 2017). The decisive factor for the stability of hematite and magnetite is the H_2 fugacity of the system (Frost, 1985). The abundance of hematite in the oxidized samples and even more so in some of the metasomatized samples, in which hematite holds

between 2/5 and 3/5 of all Fe(III), suggests that the H_2 fugacities did not cross the critical level at which hematite destabilizes and magnetite is predicted—despite the fact that H_2 is produced during the above reaction. In fact, the transformation of magnetite into hematite and/or goethite accounts for the estimated shift in H_2 production per kg rock from roughly 300–350 mmol to >400 mmol per kg rock (**Figure 7C**). It appears counterintuitive that a more oxidized assemblage comes with a high H_2 yield. But this reaction likely occurred over long timescales, presumably tens of millions of years before the seawater circulation through the basement ceased owing to the burial of the rocks by sediments (e.g., Tucholke and Sibuet, 2007). Thus, despite the fact that overall ~100 mmol H_2 per kg rock were produced during this late-stage alteration, the flux of H_2 per increment of time as well as the H_2 fugacities were presumably rather low.

We assume that the oxidation to ferric Fe would have continued and likely would have proceeded to completion if the thick layer of sediment had not restricted seawater–basement interaction. The Fe in extensively weathered serpentinites from other marine settings has been shown to be almost entirely ferric (e.g., Klein et al., 2017; Dessimoulie et al., 2020) since much of the magnetite and spinel hosting Fe(II) turned into Fe(III)-bearing hematite, goethite, and ferritchromite. The dissolution of unserpentinized olivine, serpentine, and brucite (if present) also releases ferrous Fe that is subsequently precipitated as Fe hydroxides (e.g., Jöns et al., 2017). Under the prerequisite that H_2O is the oxidizing agent, additional H_2 would be formed during each of these reactions.

H_2 Production From Continental Break-Up to Mid-Ocean Ridge Spreading

Degree of Melt Depletion at Hole 637A

Across OCTs, seawater should principally interact with SCLM at proximal and with oceanic lithospheric mantle at more distal settings. To put the findings from this communication into the context of such a transition from continental rifting and break-up to MOR spreading, we next elaborate to what extent our samples depict serpentinized SCLM. Mantle rocks consist mainly of olivine + orthopyroxene + clinopyroxene ± garnet ± spinel, the proportions of which vary with the progressive removal of basaltic components during partial melting (e.g., Arai, 1994). Lherzolites are considered to be best representative of SCLM, and persistent partial melting in response to the above-mentioned transition causes the transformation from lherzolitic (at passive margins) to harzburgitic and/or dunitic compositions (at MORs). This general change in composition occurs across the Iberia margin OCT (e.g., Hébert et al., 2001).

Geochemically, undepleted lherzolite should plot close to the primitive mantle estimates (**Figure 3**) and the rocks from the peridotite ridges at the West Iberia margin—generally thought of as variably depleted SCLM—should ideally fall along the melt depletion trend (i.e., the "terrestrial array" in Figure 2A in Niu, 2004). This is indeed the case for our as well as other Iberia margin samples. However, our samples display very heterogeneous compositions, some of which suggest little whereas others imply advanced stages of depletion. These compositions well mirror the lithological variations throughout all drill cores at the West Iberia margin, in which lherzolitic core sections can alternate with harzburgitic and dunitic ones on centimeter scales (e.g., Boillot et al., 1987; Sawyer et al., 1994; Whitmarsh et al., 1998). In addition, further heterogeneity has potentially been caused by melt infiltration (e.g., Chazot et al., 2005; Müntener and Manatschal, 2006) and/or extensive metasomatism (e.g., this study; Seifert and Brunotte, 1996). Pinning down the degree of melt depletion on the basis of our bulk compositions would hence be speculative.

A more accurate way is offered by the compositions of spinel. Prolonged melt extraction turns initially Mg- and Al-rich spinel into spinel with a higher chromite fraction, i.e., low X_{Mg} and high X_{Cr} (Arai, 1994). Spinel in our samples is particularly rich in Al and Mg and plots among the least-depleted spinels of rifted margin and MOR samples (**Figure 4A**). Further, TiO_2 contents below 0.15 wt% imply that most of our samples were not affected by significant melt impregnation processes (**Figure 4B**; cf. Müntener and Manatschal, 2006). Based on these data we infer that the investigated rocks can, overall, not have undergone large degrees of melt extraction. This interpretation is also consistent with up to 5.2 wt% Al_2O_3 in orthopyroxene and with high Al_2O_3, Na_2O, and TiO_2 contents and a high average value of 6.2 for 100*Na/(Na + Ca) for clinopyroxene (see also Evans and Girardeau, 1988). In fact, Evans and Girardeau estimated that the Site 637 peridotites have experienced less than 10% of partial melting. Based on these data and on the (reconstructed) lherzolitic protolith compositions, we are confident that the investigated rocks well resembled SCLM prior to initial serpentinization. The samples from Hole 637A hence depict a compositional endmember opposite to the dunitic and harzburgitic lithologies at MORs.

Serpentinization From Rift to Ridge

Serpentinization at Slow- and Ultraslow-Spreading Ridges

In this work we have analyzed the serpentinization and derived H_2 fluxes associated with SCLM at the most landward domain of the Iberia margin OCT. In contrast, sustained divergence led to the exposure of oceanic peridotite rather than SCLM in more oceanward domains and all along to the modern MAR. Similar transitions have been described from many settings worldwide and throughout Earth's history (e.g., Louden and Chian, 1999; Pérez-Gussinyé, 2001; Manatschal, 2004; Pérez-Gussinyé, 2006). Both rock types undergo hydration by seawater. To obtain an overview of H_2 yields across such transitions, we next review serpentinization reactions affecting oceanic mantle. We thereby explicitly focus on "background" serpentinization, i.e., pervasive hydration of the mantle that is induced by the percolation of seawater into the seafloor (contrary to serpentinization that can occur along deep faults).

We also need to take account of changing spreading rates over time. During the evolution to its present state, the MAR developed from an ultraslow- (at the OCT, about 130 Ma ago; e.g., Whitmarsh and Miles, 1995) into a slow-spreading ridge (100 s of km to the west of the OCT). Aside from the Newfoundland–Iberia conjugate margin, such increases in

extension rate have been suggested for several other break-up/spreading settings (e.g., Bullock and Minshull, 2005; Vissers et al., 2013; Williams et al., 2019). Whereas serpentinization at slow-spreading ridges is generally well understood, much less work has been conducted at their ultraslow counterparts. But previous investigations indicate that the styles of serpentinization differ between such settings.

In both cases, the extent and nature of serpentinization strongly depend on the crustal architecture, which itself is a function of variable melt supply and tectonic extension. The ultraslow-spreading Gakkel and Southwest Indian Ridges are considered to be modern counterparts of the Cretaceous MAR (cf. Whitmarsh et al., 1996; Hopper et al., 2004; Cannat et al., 2009). They are characterized by generally little magmatic activity and long stretches of sparsely to non-magmatic ridge sections separated by discontinuous volcanic centers that formed by melt focusing. Mantle blocks emplaced at the seafloor *via* detachment faulting dominate the melt-starved sections (e.g., Cannat et al., 2006; Escartín et al., 2008). Overall, the along-ridge variation in crustal thickness is immense, with little to no volcanic crust at the amagmatic sections and several kilometer thick mafic layers at volcanic centers (e.g., Jokat et al., 2003; Schmid and Schlindwein, 2016). Similarly, slow-spreading ridges are strongly segmented and melt supply at segment ends is usually low (e.g., Tolstoy et al., 1993; Detrick et al., 1995), which as well commonly results in the uplift of ultramafic seafloor to shallow depths. However, it appears that these mantle sections in many cases comprise variable volumes of gabbroic intrusions representing magma that crystallized at depth. The intrusion of such magmatic bodies results in higher pressure–temperature gradients than that expected for exhumed mantle without magmatic intrusions. Estimates for axial geotherms range from 45°C km^{-1} (Cannat et al., 2019) to 100–150°C km^{-1} (Bach et al., 2011) for magma-poor sections at slow-spreading ridges, which would place the 400°C isotherm and hence the window in which serpentinization can occur to a maximum depth of 8–9 km. Gradients at ultraslow-spreading ridges are lower, varying between about 25 and 50°C km^{-1}, depending on the magmatic activity in the respective section (Cannat et al., 2019). The depth at which serpentinization could take place would thus be extended to about 15 km. Indeed, results from microseismicity studies at the ultraslow-spreading Mid-Cayman Rise and Southwest Indian Ridge indicate extensive hydration of mantle rocks until depths of 15 km and more (Schlindwein and Schmid, 2016; Grevemeyer et al., 2019). Given that the overall amount of hydration decreases with increasing depth below seafloor (Cannat et al., 2010, proposed that significant background serpentinization does generally not extend to depths greater than 3–4 km below seafloor), these differences in the lithosphere's thermal state suggest generally lower serpentinization temperatures at ultraslow- in comparison to slow-spreading ridges. In other words, larger volumes of low-temperature serpentinite should form at ultraslow-spreading ridges—but also at rifted margins that possess similar geotherms.

This reasoning is in line with serpentinization temperature estimates from O isotope thermometry that point at much higher values for spreading systems that are magmatically active. At the MAR and Hess Deep, seawater–peridotite interaction ranges from about 200 to >400°C; those at the nonvolcanic Iberia margin are considered to have occurred at <200°C (e.g., Früh-Green et al., 2004; Barnes, et al., 2009; Klein et al., 2014).

Such distinctions presumably apply for serpentinization evoked by seawater that pervasively infiltrates the permeable basement or flows in through the ubiquitous minor faults and fractures existing in spreading systems. However, this does not exclude that higher-temperature serpentinization may also take place where geotherms are low. Detachment fault surfaces that act as fluid pathways can facilitate seawater penetration into the seafloor to depths of >10 km (e.g., deMartin et al., 2007). Such inflow likely evokes serpentinization of the detachment wall rock to proceed at great depth, i.e., at the upper end of the serpentinization temperature window (e.g., Cannat et al., 2019). Continued spreading along these detachments may cause the exposure of such high-temperature serpentine, even at ultraslow-spreading ridges. Samples collected with seafloor dredges may undoubtedly represent such former detachment surfaces and may not be representative for background serpentinization (e.g., Rouméjon et al., 2018; Tao et al., 2020).

Dependency of H_2 Yields on Rock Type and Serpentinization Temperature

The quantity of H_2 generated during serpentinization primarily depends on rock type, alteration temperature, w/r ratio, and oxidation potential of the fluid. Water/rock ratios and the nature of the fluid (usually seawater-derived) are likely similar at slow- and ultraslow-spreading ridges as well as at rifted margins. But rock types and serpentinization temperatures systematically vary between the different settings, as discussed above. In **Figure 10** we conceptualized the H_2 production potential during the evolution from continental break-up to MOR spreading.

At slow-spreading ridges, more than 80% of the H_2 generated during the serpentinization of harzburgites and dunites at temperatures in excess of 200°C originates from the formation of magnetite (Figure 5 in Klein et al., 2009). Hydrogen fluxes increase with temperature from about 200 to 350 mmol per kg of rock (dotted lines in **Figures 6D,H**); highest concentrations are expected where the maximum amounts of magnetite are formed (toward ~320°C). However, a small portion of such H_2 is generated by the oxidation of Fe that is subsequently incorporated in serpentine. Thermodynamic modeling predicts 20–35% of the Fe in serpentine to be ferrous within the temperature range of 200–280°C (Klein et al., 2009). Such serpentine compositions can be explained by mixing of serpentine–greenalite and Mg-cronstedtite (**Figure 9**); serpentine with X_{Mg} of 0.95 (as predicted by Klein et al. models) may produce about 50 mmol H_2 per kg rock. More generally, recorded serpentine compositions from MOR settings worldwide usually scatter around X_{Mg} of 0.9–0.95; no unambiguous trends toward any endmember containing ferric Fe are discernable. Even so, analyses of natural rocks from MORs (e.g., Figure 5F in Mayhew and Ellison, 2020) suggest that up to 2/3 of the Fe in serpentine can be ferric. Such increase in Fe(III)/$\sum$Fe would raise the amounts of H_2 generated solely by serpentine

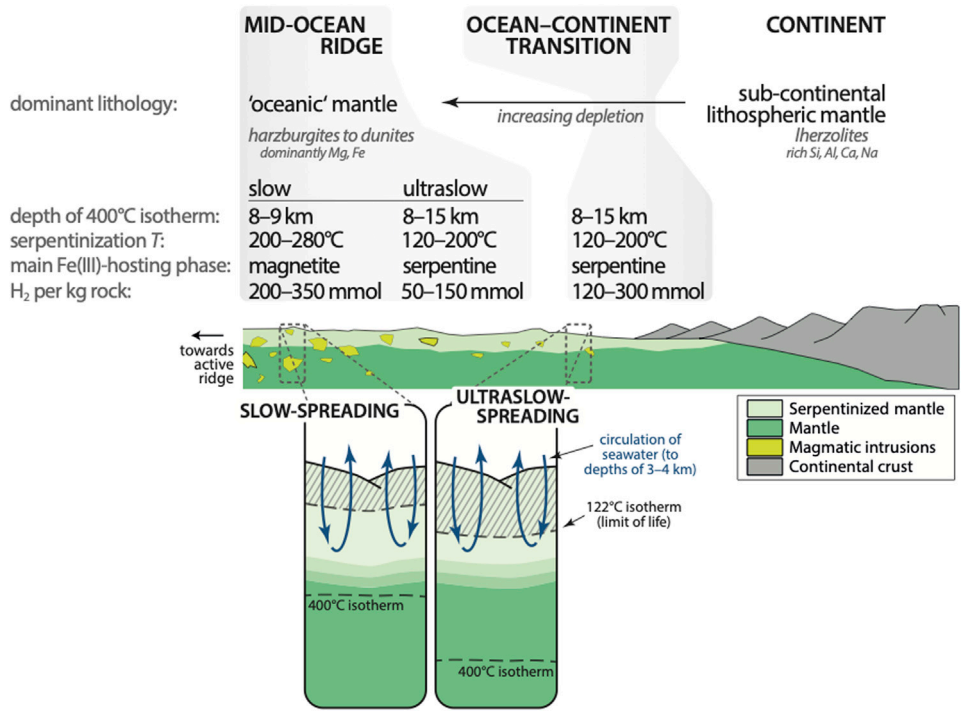

FIGURE 10 | Conceptual sketch of serpentinization-related H_2 production from rift to ridge (active MOR toward the left). These general changes in H_2 production likely apply to the majority of magma-poor rifted margins as well as ultraslow- and slow-spreading MORs. Lithological changes and variations in geotherms, the latter being strongly dependent on the extension rates, result in distinct serpentinization phase assemblages. At ultraslow rates, large volumes of serpentinite should produce H_2 under conditions close to/within the habitable zone (lower right inset). See main text for further discussion. Limit of life after Takai et al. (2008).

to levels of ~180 mmol per kg rock (**Figure 9**). Microprobe data plotted on the frequently-used SiO_2–FeO–MgO plane would not reveal such high Fe(III) contents.

In contrast, H_2 generation at ultraslow-spreading ridges should be mainly driven by Fe(III)-serpentine because of considerably lower serpentinization temperatures. In fact, thermodynamic modeling predicts magnetite-free mineral assemblages at temperatures below ~160°C (Klein et al., 2009). If a little more than 20% of the Fe in serpentine were ferric (Figure 5B in Klein et al., 2009), such rocks would produce between about 50 and 100 mmol H_2 for X_{Mg} values of 0.95 and 0.9, respectively (**Figure 9**). Higher Fe(III)/∑Fe in serpentine would considerably increase the levels of H_2 (see above). The serpentinized harzburgites and dunites recovered from the distal parts of the Iberia margin OCT can be considered as examples for ultraslow-spreading MORs; these rocks hold very little magnetite owing to rather low serpentinization temperatures and, instead, the Fe partitioned into brucite (Agrinier et al., 1996; Beard and Hopkinson, 2000; Klein et al., 2014).

In the proximal parts of OCTs, where the exposed mantle is rather lherzolitic in nature, background serpentinization also occurs at low temperatures and the main driver for H_2 production is Fe(III)-rich serpentine. The presence of such cronstedtite-rich serpentine is promoted by rather high $aSiO_2$ during the serpentinization of pyroxene-rich peridotite (in comparison to the alteration of harzburgites and dunites at MORs; **Figure 8**). Our results imply that considerable amounts of H_2 can be produced. With about 2/3 of the Fe being ferric in our least-modified samples, >300 mmol H_2 per kg serpentinite may have been generated (**Figure 7C**). This value is much higher in comparison to ultraslow-spreading ridges and similar to magnetite-dominated high-temperature serpentinization at slow-spreading ridges. Considering that not all of the oxidation of these samples has been caused by seawater, the true H_2 yields may have been somewhat lower. But even with H_2O as the only oxidant, ~120–160 mmol H_2 per kg rock are thermodynamically realistic (**Figures 6D,H**) and can be considered as an absolute minimum estimate.

Magnetic properties of drilled serpentinites support our conjecture that H_2 yields can predominantly be ascribed to magnetite at slow-spreading ridges but not at magma-poor systems. Comparing serpentinite magnetic susceptibilities reveals the abundance of magnetite at the slow-spreading MAR and thus highlights the distinction in the alteration mineral assemblages in comparison to the West Iberia margin (**Figure 11**). Serpentinization at the MAR can produce large amounts of magnetite and consequently forms rocks with high albeit variable magnetic susceptibilities. Since the production of magnetite enhances with the degree of serpentinization, magnetic susceptibilities increase rapidly when the degree of alteration exceeds 75% (Toft et al., 1990; Oufi et al., 2002). In this regard, Oufi et al. suggested a threshold at about 0.05 SI that separates weakly from extensively serpentinized samples (dashed gray bar in **Figure 11**; see also Figure 5C in Maffione et al., 2014). By contrast, recovery from the Iberia and Newfoundland margins

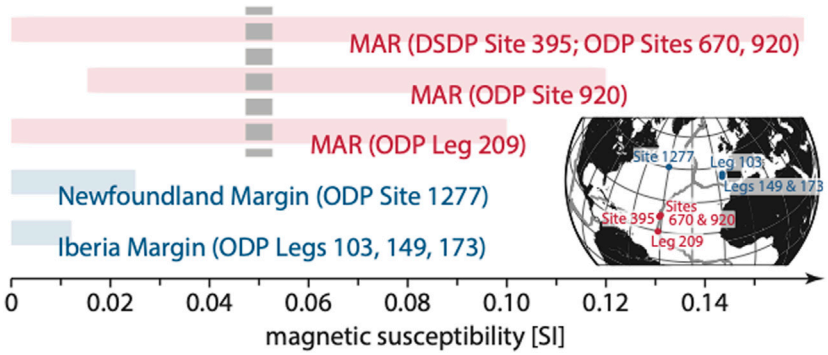

FIGURE 11 | Magnetic susceptibilities of drilled serpentinites. At magma-poor margins, magnetic susceptibilities of extensively serpentinized rocks are low; those in rocks from the MAR are generally much higher. Since magnetite formation increases with temperature, the high magnetic susceptibilities of the MAR rocks are indicative of serpentinization that took place in excess of 200°C. MAR samples with magnetic susceptibilities <0.05 SI (dashed gray bar) likely relate to samples with low degrees of alteration (the amount of magnetite correlates with the degree of serpentinization; see Oufi et al., 2002) or may mirror late-stage serpentinization at lower temperatures (e.g., Bonnemains et al., 2016) or alteration of magnetite to maghemite (Oufi et al., 2002). This figure includes data from Boillot et al. (1987), Sawyer et al. (1994), Whitmarsh et al. (1998), Oufi et al. (2002), Kelemen et al. (2004), Tucholke et al. (2004), Klein et al. (2014), Bonnemains et al. (2016). We only considered ultramafic cores with no/little fault gouge from ODP Leg 209, i.e., Cores 2R–11R, 18R, 19R, 24R of Hole 1268A; 1R, 2R, 4R of Hole 1270A; 1R–3M of Hole 1270C; 11R of Hole 1270D; 6R of Hole 1271A; 2R, 7R, 18R of Hole 1271B; 12R, 14R, 16R–21R, 23R–27R of Hole 1272A; 1R–17R, 27R of Hole 1274A.

exhibits low magnetic susceptibilities, even though it is extensively serpentinized. Long-lasting weathering of these rocks at the seafloor may have obscured the initial magnetite contents to a certain degree but our results demonstrate that at least the least modified samples well reflect initial serpentinization products. The magnetite contents of these samples are, however, also low.

In addition to H_2 produced by serpentine (and magnetite), the formation of garnet during serpentinization may even increase H_2 yields at sites of continental break-up and at OCTs. Our thermodynamic calculations predict up to 8 vol% garnet dominated by an andradite component for lherzolitic rocks (**Supplementary Figure S7**). Its formation would raise the levels of H_2(aq) to ~100–170 mmol at temperatures below ~250°C, which is an increase by a factor of two to three in comparison to serpentinization of dunites and/or harzburgites (**Supplementary Figures S7D,H**). At the Iberia margin, andradite and hydroandradite have indeed been observed at Site 1068 (e.g., Beard and Hopkinson, 2000).

At both rifts and ridges, late-stage alteration of serpentinites produces further H_2 flux to the ocean. Since serpentinized dunites and harzburgites possess generally larger pools of Fe(II) in comparison to lherzolites (Fe(III)/∑Fe = 0.57 and 0.58 vs. 0.65, respectively; Mayhew and Ellison, 2020) their potential for H_2 production during weathering is slightly larger. Low-temperature weathering and the related mineralogical and geochemical changes are presumably long-lasting, widespread, and hence even more important at MORs (over OCTs) because sedimentation rates at these settings are usually lower and inefficiently inhibit seawater–serpentinite interactions.

CONCLUSION

Hydrogen yields during seawater–peridotite interactions primarily rely on the serpentinization mineral assemblages, which in turn strongly depend on protolith type and alteration temperature. During the evolution from continental rifting and break-up affecting Pangea to MOR spreading in the North Atlantic, a succession of lherzolitic to harzburgitic and dunitic rocks underwent serpentinization—at low temperatures (<200°C) during rifting and early, ultraslow spreading and at higher temperatures (200–280°C) during later spreading at slow rates. During low-temperature serpentinization, the incorporation of Fe(III) in serpentine was mainly responsible for H_2 production. Hydrogen yields were likely higher by a factor of two or more during the seawater–lherzolite reactions at the OCT in comparison to those resulting from the hydration of harzburgites/dunites at the early, ultraslow-spreading MAR, because much ferrous Fe was partitioned into brucite in the latter. Once higher geotherms and thus higher serpentinization temperatures were established, the formation of larger amounts of magnetite again increased the H_2 formation. Continued weathering during cold, late-stage weathering of the serpentinites at the seafloor caused additional H_2 fluxes to the ocean.

These concepts and general changes in H_2 production likely apply to the majority of magma-poor margins as well as ultraslow- and slow-spreading MORs. We speculate that sufficient catabolic energy (in the form of H_2) is available at magma-poor rifted margins and ultraslow-spreading ridges to enable lithoautotrophic life (see discussion by Lang and Brazelton, 2020). Indeed, particularly large volumes of serpentinite should form at temperatures close to those at/below the limit of life (**Figure 10**), which likely favors geological–biological interactions and the presence of a hydrogenotrophy-based biosphere.

DATA AVAILABILITY STATEMENT

The original contributions presented in the study are included in the article/**Supplementary Material**, further inquiries can be directed to the corresponding author.

AUTHOR CONTRIBUTIONS

EA and MP-G designed the study. EA re-sampled the drill cores, investigated the samples, and conducted the analyses, except for magnetometry (TF) and Mössbauer spectroscopy (CM). EA and WB performed the modeling. EA wrote the manuscript with contributions from all co-authors.

FUNDING

This project was funded by the Helmholtz Association 'POSY – The Polar System and its Effects on the Ocean Floor' (project no. ExNet-0001-Phase2-3).

ACKNOWLEDGMENTS

This research used samples and data provided by ODP. We are grateful to the captain and crew of the *JOIDES* Resolution and to the members of the Science Party. Eleonore Gründken, Bernhard Schnetger, and Brit Kokisch are thanked for help with bulk rock geochemical analyses, and Frieder Klein for Raman spectroscopy. We greatly appreciate editorial handling by MG and constructive reviews by OM and CB that helped to improve earlier versions of this manuscript.

SUPPLEMENTARY MATERIAL

The Supplementary Material for this article can be found online at: https://www.frontiersin.org/articles/10.3389/feart.2021.673063/full#supplementary-material

REFERENCES

Abe, N. (2001). Petrochemistry of Serpentinized Peridotite from the Iberia Abyssal Plain (ODP Leg 173): its Character Intermediate between Suboceanic and Subcontinental Upper Mantle. *Geol. Soc. Lond. Spec. Publications* 187, 143–159. doi:10.1144/gsl.sp.2001.187.01.08

Agrinier, P., Cornen, G., and Beslier, M.-O. (1996). "Mineralogical and Oxygen Isotopic Features of Serpentinites Recovered from the Ocean/continent Transition in the Iberia Abyssal Plain," in *Proceedings of the Ocean Drilling Program, 149 Scientific Results*. Editors R. B. Whitmarsh, D. S. Sawyer, A. Klaus, and D. G. Masson (College Station: TX (Ocean Drilling Program)), 541–552. doi:10.2973/odp.proc.sr.149.223.1996

Agrinier, P., Mével, C., and Girardeau, J. (1988). "Hydrothermal Alteration of the Peridotites Cored at the Ocean/Continent Boundary of the Iberian Margin: Petrologic and Stable Isotope Evidence," in *Proceedings of the Ocean Drilling Program, 103 Scientific Results*. Editors G. Boillot and E. L. Winterer (College Station: TX (Ocean Drilling Program)), 225–234. doi:10.2973/odp.proc.sr.103.136.1988

Andreani, M., Muñoz, M., Marcaillou, C., and Delacour, A. (2013). μXANES Study of Iron Redox State in Serpentine during Oceanic Serpentinization. *Lithos* 178, 70–83. doi:10.1016/j.lithos.2013.04.008

Arai, S. (1994). Characterization of Spinel Peridotites by Olivine-Spinel Compositional Relationships: Review and Interpretation. *Chem. Geology* 113, 191–204. doi:10.1016/0009-2541(94)90066-3

Bach, W., Paulick, H., Garrido, C. J., Ildefonse, B., Meurer, W. P., and Humphris, S. E. (2006). Unraveling the Sequence of Serpentinization Reactions: Petrography, mineral Chemistry, and Petrophysics of Serpentinites from MAR 15°N (ODP Leg 209, Site 1274). *Geophys. Res. Lett.* 33 (13), L13306. doi:10.1029/2006gl025681

Bach, W., Rosner, M., Jöns, N., Rausch, S., Robinson, L. F., Paulick, H., et al. (2011). Carbonate Veins Trace Seawater Circulation during Exhumation and Uplift of Mantle Rock: Results from ODP Leg 209. *Earth Planet. Sci. Lett.* 311, 242–252. doi:10.1016/j.epsl.2011.09.021

Barnes, J. D., Paulick, H., Sharp, Z. D., Bach, W., and Beaudoin, G. (2009). Stable Isotope (δ18O, δD, δ37Cl) Evidence for Multiple Fluid Histories in Mid-Atlantic Abyssal Peridotites (ODP Leg 209). *Lithos* 110, 83–94. doi:10.1016/j.lithos.2008.12.004

Barnes, J. D., and Sharp, Z. D. (2006). Achlorine Isotope Study of DSDP/ODP Serpentinized Ultramafic Rocks: Insights into the Serpentinization Process. *Chem. Geology.* 228, 246–265. doi:10.1016/j.chemgeo.2005.10.011

Bayrakci, G., Minshull, T. A., Sawyer, D. S., Reston, T. J., Klaeschen, D., Papenberg, C., et al. (2016). Fault-controlled Hydration of the Upper Mantle during continental Rifting. *Nat. Geosci* 9, 384–388. doi:10.1038/ngeo2671

Beard, J. S., and Hopkinson, L. (2000). A Fossil, Serpentinization-Related Hydrothermal Vent, Ocean Drilling Program Leg 173, Site 1068 (Iberia Abyssal Plain): Some Aspects of mineral and Fluid Chemistry. *J. Geophys. Res.* 105 (B7), 16527–16539. doi:10.1029/2000jb900073

Beslier, M.-O., Whitmarsh, R. B., Wallace, P. J., and Girardeau, J. (2001). *Proc. ODP, Sci. Results, 173*. College Station: TX (Ocean Drilling Program). doi:10.2973/odp.proc.sr.173.2001

Bodinier, J.-L., and Godard, M. (2014). "Orogenic, Ophiolitic, and Abyssal Peridotites," in *Treatise on Geochemistry*. Editors H. D. Holland and K. K. Turekian (Oxford: Elsevier), 103–167. doi:10.1016/b978-0-08-095975-7.00204-7

Boillot, G., Winterer, E. L., and Meyer, A. W. (1987). *Proceedings of the Ocean Drilling Program, 103 Initial Reports*. Repts., 103. College Station: TX (Ocean Drilling Program). doi:10.2973/odp.proc.ir.103.1987

Boillot, G., and Winterer, E. L. (1988). *Proceedings of the Ocean Drilling Program, 103 Scientific Results*. Results, 103. College Station: TX (Ocean Drilling Program). doi:10.2973/odp.proc.sr.103.1988

Bonnemains, D., Carlut, J., Escartín, J., Mével, C., Andreani, M., and Debret, B. (2016). Magnetic Signatures of Serpentinization at Ophiolite Complexes. *Geochem. Geophys. Geosyst.* 17 (8), 2969–2986. doi:10.1002/2016gc006321

Brun, J. P., and Beslier, M. O. (1996). Mantle Exhumation at Passive Margins. *Earth Planet. Sci. Lett.* 142 (1–2), 161–173. doi:10.1016/0012-821x(96)00080-5

Bullock, A. D., and Minshull, T. A. (2005). From continental Extension to Seafloor Spreading: Crustal Structure of the Goban Spur Rifted Margin, Southwest of the UK. *Geophys. J. Int.* 163, 527–546. doi:10.1111/j.1365-246x.2005.02726.x

Cannat, M., Fontaine, F., and Escartín, J. (2010). Serpentinization and Associated Hydrogen and Methane Fluxes at Slow Spreading Ridges. *Geophys. Monogr. Ser.* 188, 241–264. doi:10.1029/2008gm000760

Cannat, M., Manatschal, G., Sauter, D., and Péron-Pinvidic, G. (2009). Assessing the Conditions of continental Breakup at Magma-Poor Rifted Margins: what Can We Learn from Slow Spreading Mid-ocean Ridges? *Comptes Rendus Geosci.* 341 (5), 406–427. doi:10.1016/j.crte.2009.01.005

Cannat, M., Sauter, D., Lavier, L., Bickert, M., Momoh, E., and Leroy, S. (2019). On Spreading Modes and Magma Supply at Slow and Ultraslow Mid-ocean Ridges. *Earth Planet. Sci. Lett.* 519, 223–233. doi:10.1016/j.epsl.2019.05.012

Cannat, M., Sauter, D., Mendel, V., Ruellan, E., Okino, K., Escartín, J., et al. (2006). Modes of Seafloor Generation at a Melt-Poor Ultraslow-Spreading ridge. *Geol* 34 (7), 605–608. doi:10.1130/g22486.1

Chazot, G., Charpentier, S., Kornprobst, J., Vannucci, R., and Luais, B. (2005). Lithospheric Mantle Evolution during continental Break-Up: the West Iberia Non-volcanic Passive Margin. *J. Petrol.* 46 (12), 2527–2568. doi:10.1093/petrology/egi064

Cornen, G., Beslier, M.-O., and Girardeau, J. (1996). "Petrologic Characteristics of the Ultramafic Rocks from the Ocean/continent Transition in the Iberia Abyssal plain," in *Proceedings of the Ocean Drilling Program, 149 Scientific Results*. Editors R. B. Whitmarsh, D. S. Sawyer, A. Klaus, and D. G. Masson (College Station: TX (Ocean Drilling Program)), 377–395. doi:10.2973/odp.proc.sr.149.215.1996

Dean, S. L., Sawyer, D. S., and Morgan, J. K. (2015). Galicia Bank Ocean-Continent Transition Zone: New Seismic Reflection Constraints. *Earth Planet. Sci. Lett.* 413, 197–207. doi:10.1016/j.epsl.2014.12.045

Dean, S. M., Minshull, T. A., Whitmarsh, R. B., and Louden, K. E. (2000). Deep Structure of the Ocean-Continent Transition in the Southern Iberia Abyssal Plain from Seismic Refraction Profiles: The IAM-9 Transect at 40°20′N. *J. Geophys. Res.* 105 (B3), 5859–5885. doi:10.1029/1999jb900301

deMartin, B. J., Sohn, R. A., Canales, J. P., and Humphris, S. E. (2007). Kinematics and Geometry of Active Detachment Faulting beneath the Trans-Atlantic Geotraverse (TAG) Hydrothermal Field on the Mid-Atlantic Ridge. *Geology* 35 (8), 711–714. doi:10.1130/g23718a.1

Dessimoulie, L., Delacour, A., Guillaume, D., Chevet, J., and Cottin, J.-Y. (2020). Major and Trace Elements Exchanges during Fluid-Rock Interaction at Ultraslow-Spreading Oceanic Lithosphere: Example of the South West Indian Ridge (SWIR). *Lithos* 352-353, 105233. doi:10.1016/j.lithos.2019.105233

Detrick, R. S., Needham, H. D., and Renard, V. (1995). Gravity Anomalies and Crustal Thickness Variations along the Mid-Atlantic Ridge between 33°N and 40°N. *J. Geophys. Res.* 100 (B3), 3767–3787. doi:10.1029/94jb02649

Dunlop, D. J., and Özdemir, Ö. (1997). *Rock Magnetism: Fundamentals and Frontiers*. Cambridge: Cambridge Univ. Press, 1–573. doi:10.1017/cbo9780511612794

Eckert, S., Brumsack, H.-J., Severmann, S., Schnetger, B., März, C., and Fröllje, H. (2013). Establishment of Euxinic Conditions in the Holocene Black Sea. *Geology* 41 (4), 431–434. doi:10.1130/g33826.1

Edwards, K. J., Bach, W., and McCollom, T. M. (2005). Geomicrobiology in Oceanography: Microbe-mineral Interactions at and below the Seafloor. *Trends Microbiol.* 13 (9), 449–456. doi:10.1016/j.tim.2005.07.005

Escartín, J., Smith, D. K., Cann, J., Schouten, H., Langmuir, C. H., and Escrig, S. (2008). Central Role of Detachment Faults in Accretion of Slow-Spreading Oceanic Lithosphere. *Nature* 455, 790–794. doi:10.1038/nature07333

Evans, B. W., Hattori, K., and Baronnet, A. (2013). Serpentinite: What, why, where? *Elements* 9 (2), 99–106. doi:10.2113/gselements.9.2.99

Evans, C. A., and Baltuck, M. (1988). "Low-Temperature Alteration of Peridotite, Hole 637A," in *Proceedings of the Ocean Drilling Program, 103 Scientific Results*. Editors G. Boillot and E. L. Winterer (College Station: TX (Ocean Drilling Program)), 235–239. doi:10.2973/odp.proc.sr.103.139.1988

Evans, C. A., and Girardeau, J. (1988). "Galicia Margin Peridotites: Undepleted Abyssal Periodotites from the North Atlantic," in *Proceedings of the Ocean Drilling Program, 103 Scientific Results*. Editors G. Boillot and E. L. Winterer (College Station: TX (Ocean Drilling Program)), 195–207. doi:10.2973/odp.proc.sr.103.138.1988

Flanders, P. J. (1988). An Alternating-gradient Magnetometer (Invited). *J. Appl. Phys.* 63 (8), 3940–3945. doi:10.1063/1.340582

Frost, B. R., and Beard, J. S. (2007). On Silica Activity and Serpentinization. *J. Pet.* 48 (7), 1351–1368. doi:10.1093/petrology/egm021

Frost, B. R. (1985). On the Stability of Sulfides, Oxides, and Native Metals in Serpentinite. *J. Pet.* 26, 31–63. doi:10.1093/petrology/26.1.31

Früh-Green, G. L., Connolly, J. A. D., Plas, A., Kelley, D. S., and Grobéty, B. (2004). Serpentinization of Oceanic Peridotites: Implications for Geochemical Cycles and Biological Activity. *Geophys. Monogr. Ser.* 144, 119–136. doi:10.1029/144gm08

Fryer, P., Wheat, C. G., Williams, T., Kelley, C., Johnson, K., Ryan, J., et al. (2020). Mariana Serpentinite Mud Volcanism Exhumes Subducted Seamount Materials: Implications for the Origin of Life. *Phil. Trans. R. Soc. A.* 378, 20180425. doi:10.1098/rsta.2018.0425

Gibson, I. L., Beslier, M.-O., Cornen, G., Milliken, K. L., and Seifert, K. E. (1996). "Major- and Trace Element Seawater Alteration Profiles in Serpentinite Formed during the Development of the Iberia Margin, Site 897," in *Proceedings of the Ocean Drilling Program, 149 Scientific Results*. Editors R. B. Whitmarsh, D. S. Sawyer, A. Klaus, and D. G. Masson (College Station: TX (Ocean Drilling Program)), 519–527. doi:10.2973/odp.proc.sr.149.219.1996

Godard, M., Lagabrielle, Y., Alard, O., and Harvey, J. (2008). Geochemistry of the Highly Depleted Peridotites Drilled at ODP Sites 1272 and 1274 (Fifteen-Twenty Fracture Zone, Mid-Atlantic Ridge): Implications for Mantle Dynamics beneath a Slow Spreading ridge. *Earth Planet. Sci. Lett.* 267 (3–4), 410–425. doi:10.1016/j.epsl.2007.11.058

Grevemeyer, I., Hayman, N. W., Lange, D., Peirce, C., Papenberg, C., Van Avendonk, H. J. A., et al. (2019). Constraining the Maximum Depth of Brittle Deformation at Slow- and Ultraslow-Spreading Ridges Using Microseismicity. *Geology* 47, 1069–1073. doi:10.1130/g46577.1

Hébert, R., Gueddari, K., LaFlèche, M. R., Beslier, M.-O., and Gardien, V. (2001). Petrology and Geochemistry of Exhumed Peridotites and Gabbros at Non-volcanic Margins: ODP Leg 173 West Iberia Ocena-Continent Transition Zone. *Geol. Soc. Lond. Spec. Publications* 187, 161–189. doi:10.1144/gsl.sp.2001.187.01.09

Hellebrand, E., Snow, J. E., and Mühe, R. (2002). Mantle Melting beneath Gakkel Ridge (Arctic Ocean): Abyssal Peridotite Spinel Compositions. *Chem. Geol.* 182 (2), 227–235. doi:10.1016/s0009-2541(01)00291-1

Hofmann, A. W. (1988). Chemical Differentiation of the Earth: the Relationship between Mantle, Continental Crust, and Oceanic Crust. *Earth Planet. Sci. Lett.* 90 (3), 297–314. doi:10.1016/0012-821x(88)90132-x

Hopkinson, L., Beard, J. S., and Boulter, C. A. (2004). The Hydrothermal Plumbing of a Serpentinite-Hosted Detachment: Evidence from the West Iberia Non-volcanic Rifted continental Margin. *Mar. Geol.* 204 (3–4), 301–315. doi:10.1016/s0025-3227(03)00374-8

Hopper, J. R., Funck, T., Tucholke, B. E., Christian Larsen, H., Holbrook, W. S., Louden, K. E., et al. (2004). Continental Breakup and the Onset of Ultraslow Seafloor Spreading off Flemish Cap on the Newfoundland Rifted Margin. *Geol* 32 (1), 93. doi:10.1130/g19694.1

Jarosewich, E., Nelen, J. A., and Norberg, J. A. (1980). Reference Samples for Electron Microprobe Analysis*. *Geostandard Newslett.* 4 (1), 43–47. doi:10.1111/j.1751-908x.1980.tb00273.x

Johnson, J. W., Oelkers, E. H., and Helgeson, H. C. (1992). SUPCRT92: A Software Package for Calculating the Standard Molal Thermodynamic Properties of Minerals, Gases, Aqueous Species, and Reactions from 1 to 5000 Bar and 0 to 1000°C. *Comput. Geosciences* 18 (7), 899–947. doi:10.1016/0098-3004(92)90029-q

Jokat, W., Ritzmann, O., Schmidt-Aursch, M. C., Drachev, S., Gauger, S., and Snow, J. (2003). Geophysical Evidence for Reduced Melt Production on the Arctic Ultraslow Gakkel Mid-ocean ridge. *Nature* 423 (6943), 962–965. doi:10.1038/nature01706

Jöns, N., Bach, W., and Klein, F. (2010). Magmatic Influence on Reaction Paths and Element Transport during Serpentinization. *Chem. Geology.* 274 (3–4), 196–211. doi:10.1016/j.chemgeo.2010.04.009

Jöns, N., Kahl, W.-A., and Bach, W. (2017). Reaction-induced Porosity and Onset of Low-Temperature Carbonation in Abyssal Peridotites: Insights from 3D High-Resolution Microtomography. *Lithos* 268-271, 274–284. doi:10.1016/j.lithos.2016.11.014

Kelemen, P. B., Kikawa, E., and Miller, D. J. (2004). *Proceedings of the Ocean Drilling Program, 209 Initial Reports*. Repts., 209. College Station: TX (Ocean Drilling Program). doi:10.2973/odp.proc.ir.209.2004

Kimball, K. L., and Evans, C. A. (1988). "Hydrothermal Alteration of Peridotite from the Galicia Margin, Iberian Peninsula," in *Proceedings of the Ocean Drilling Program, 103 Scientific Results*. Editors G. Boillot and E. L. Winterer (College Station: TX (Ocean Drilling Program)), 241–251. doi:10.2973/odp.proc.sr.103.140.1988

Klein, F., Bach, W., Humphris, S. E., Kahl, W.-A., Jöns, N., Moskowitz, B., et al. (2014). Magnetite in Seafloor Serpentinite--Some like it Hot. *Geology* 42 (2), 135–138. doi:10.1130/g35068.1

Klein, F., Bach, W., Jöns, N., McCollom, T., Moskowitz, B., and Berquó, T. (2009). Iron Partitioning and Hydrogen Generation during Serpentinization of Abyssal Peridotites from 15°N on the Mid-Atlantic Ridge. *Geochimica et Cosmochimica Acta* 73 (22), 6868–6893. doi:10.1016/j.gca.2009.08.021

Klein, F., Bach, W., and McCollom, T. M. (2013). Compositional Controls on Hydrogen Generation during Serpentinization of Ultramafic Rocks. *Lithos* 178, 55–69. doi:10.1016/j.lithos.2013.03.008

Klein, F., Humphris, S. E., and Bach, W. (2020). Brucite Formation and Dissolution in Oceanic Serpentinite. *Geochem. Persp. Let.* 16, 1–5. doi:10.7185/geochemlet.2035

Klein, F., Humphris, S. E., Guo, W., Schubotz, F., Schwarzenbach, E. M., and Orsi, W. D. (2015). Fluid Mixing and the Deep Biosphere of a Fossil Lost City-type

Hydrothermal System at the Iberia Margin. *Proc. Natl. Acad. Sci. USA* 112 (39), 12036–12041. doi:10.1073/pnas.1504674112

Klein, F., Marschall, H. R., Bowring, S. A., Humphris, S. E., and Horning, G. (2017). Mid-ocean ridge Serpentinite in the Puerto Rico Trench: from Seafloor Spreading to Subduction. *J. Petrol.* 58 (9), 1729–1754. doi:10.1093/petrology/egx071

Kodolányi, J., Pettke, T., Spandler, C., Kamber, B. S., and Gméling, K. (2012). Geochemistry of Ocean Floor and Fore-Arc Serpentinites: Constraints on the Ultramafic Input to Subduction Zones. *J. Petrol.* 53 (2), 235–270. doi:10.1093/petrology/egr058

Lang, S. Q., and Brazelton, W. J. (2020). Habitability of the marine Serpentinite Subsurface: a Case Study of the Lost City Hydrothermal Field. *Phil. Trans. R. Soc. A.* 378, 20180429. doi:10.1098/rsta.2018.0429

Louden, K. E., and Chian, D. (1999). The Deep Structure of Non-volcanic Rifted Continental Margins. *Phil. Trans. R. Soc. A.* 357, 767–804. doi:10.1098/rsta.1999.0352

Maffione, M., Morris, A., Plümper, O., and van Hinsbergen, D. J. J. (2014). Magnetic Properties of Variably Serpentinized Peridotites and Their Implication for the Evolution of Oceanic Core Complexes. *Geochem. Geophys. Geosyst.* 15 (4), 923–944. doi:10.1002/2013gc004993

Manatschal, G., Froitzheim, N., Rubenach, M., and Turrin, B. D. (2001). The Role of Detachment Faulting in the Formation of an Ocean-Continent Transition: Insights from the Iberia Abyssal Plain. *Geol. Soc. Lond. Spec. Publications* 187 (1), 405–428. doi:10.1144/gsl.sp.2001.187.01.20

Manatschal, G. (2004). New Models for Evolution of Magma-Poor Rifted Margins Based on a Review of Data and Concepts from West Iberia and the Alps. *Int. J. Earth Sci. (Geol Rundsch)* 93, 432–466. doi:10.1007/s00531-004-0394-7

Mayhew, L. E., and Ellison, E. T. (2020). A Synthesis and Meta-Analysis of the Fe Chemistry of Serpentinites and Serpentine Minerals. *Phil. Trans. R. Soc. A.* 378, 20180420. doi:10.1098/rsta.2018.0420

McCollom, T. M., and Bach, W. (2009). Thermodynamic Constraints on Hydrogen Generation during Serpentinization of Ultramafic Rocks. *Geochimica et Cosmochimica Acta* 73 (3), 856–875. doi:10.1016/j.gca.2008.10.032

McCollom, T. M., Klein, F., Moskowitz, B., Berquó, T. S., Bach, W., and Templeton, A. S. (2020). Hydrogen Generation and Iron Partitioning during Experimental Serpentinization of an Olivine-Pyroxene Mixture. *Geochimica et Cosmochimica Acta* 282, 55–75. doi:10.1016/j.gca.2020.05.016

McCollom, T. M., and Seewald, J. S. (2013). Serpentinites, Hydrogen, and Life. *Elements* 9 (2), 129–134. doi:10.2113/gselements.9.2.129

McDonough, W. F., and Sun, S.-s. (1995). The Composition of the Earth. *Chem. Geol.* 120 (3–4), 223–253. doi:10.1016/0009-2541(94)00140-4

Moll, M., Paulick, H., Suhr, G., and Bach, W. (2007). "Data Report: Microprobe Analyses of Primary Phases (Olivine, Pyroxene, and Spinel) and Alteration Products (Serpentine, Iowaite, Talc, Magnetite, and Sulfides) in Holes 1268A, 1272A, and 1274A," in *Proceedings of the Ocean Drilling Program, 209 Scientific Results*. Editors P. B. Kelemen, E. Kikawa, and D. J. Miller (College Station: TX (Ocean Drilling Program)), 1–13. doi:10.2973/odp.proc.sr.209.003.2007

Müntener, O., and Manatschal, G. (2006). High Degrees of Melt Extraction Recorded by Spinel Harzburgite of the Newfoundland Margin: the Role of Inheritance and Consequences for the Evolution of the Southern North Atlantic. *Earth Planet. Sci. Lett.* 252 (3–4), 437–452. doi:10.1016/j.epsl.2006.10.009

Niu, Y. (2004). Bulk-rock Major and Trace Element Compositions of Abyssal Peridotites: Implications for Mantle Melting Melt Extraction and post-melting Processes beneath Mid-ocean Ridges. *J. Petrol.* 45 (12), 2423–2458. doi:10.1093/petrology/egh068

Obeso, J. C., and Kelemen, P. B. (2020). Major Element Mobility during Serpentinization, Oxidation and Weathering of Mantle Peridotite at Low Temperatures. *Phil. Trans. R. Soc. A.* 378, 20180433. doi:10.1098/rsta.2018.0433

O'Hanley, D. S., and Dyar, M. D. (1993). The Composition of Lizardite 1T and the Formation of Magnetite in Serpentinites. *Am. Mineral.* 78, 391–404.

Oufi, O., Cannat, M., and Horen, H. (2002). Magnetic Properties of Variably Serpentinized Abyssal Peridotites. *J. Geophys. Res.* 107 (B5), 2095. doi:10.1029/2001jb000549

Özdemir, Ö., and Dunlop, D. J. (2010). Hallmarks of Maghemitization in Low-Temperature Remanence Cycling of Partially Oxidized Magnetite Nanoparticles. *J. Geophys. Res. Solid Earth* 115, B02101. doi:10.1029/2009jb006756

Pérez-Gussinyé, M. (2012). A Tectonic Model for Hyperextension at Magma-Poor Rifted Margins: an Example from the West Iberia–Newfoundland Conjugate Margins. *Geol. Soc. Spec. Pub.* 369 (1), 403–427. doi:10.1144/sp369.19

Pérez-Gussinyé, M., Morgan, J. P., Reston, T. J., and Ranero, C. R. (2006). The Rift to Drift Transition at Non-volcanic Margins: Insights from Numerical Modelling. *Earth Planet. Sci. Lett.* 244 (1–2), 458–473. doi:10.1016/j.epsl.2006.01.059

Pérez-Gussinyé, M., and Reston, T. J. (2001). Rheological Evolution during Extension at Nonvolcanic Rifted Margins: Onset of Serpentinization and Development of Detachments Leading to continental Breakup. *J. Geophys. Res.* 106 (B3), 3961–3975. doi:10.1029/2000jb900325

Petersen, J. M., Zielinski, F. U., Pape, T., Seifert, R., Moraru, C., Amann, R., et al. (2011). Hydrogen Is an Energy Source for Hydrothermal Vent Symbioses. *Nature* 476, 176–180. doi:10.1038/nature10325

Pickup, S. L. B., Whitmarsh, R. B., Fowler, C. M. R., and Reston, T. J. (1996). Insight into the Nature of the Ocean-Continent Transition off West Iberia from a Deep Multichannel Seismic Reflection Profile. *Geology* 24 (12), 1079–1082. doi:10.1130/0091-7613(1996)024<1079:iitnot>2.3.co;2

Prescher, C., McCammon, C., and Dubrovinsky, L. (2012). MossA: a Program for Analyzing Energy-Domain Mössbauer Spectra from Conventional and Synchrotron Sources. *J. Appl. Crystallog.* 45, 329–331. doi:10.1107/s0021889812004979

Reston, T. J., and McDermott, K. G. (2011). Successive Detachment Faults and Mantle Unroofing at Magma-Poor Rifted Margins. *Geology* 39, 1071–1074. doi:10.1130/g32428.1

Rouméjon, S., Williams, M. J., and Früh-Green, G. L. (2018). *In-situ* Oxygen Isotope Analyses in Serpentine Minerals: Constraints on Serpentinization during Tectonic Exhumation at Slow- and Ultraslow-Spreading Ridges. *Lithos* 323, 156–173. doi:10.1016/j.lithos.2018.09.021

Sakharov, B. A., Dubińska, E., Bylina, P., Kozubowski, J. A., Kapron, G., and Frontczak-Baniewicz, M. (2004). Serpentine-smectite Interstratified Minerals from Lower Silesia (SW Poland). *Clays Clay Miner.* 52 (1), 55–65. doi:10.1346/ccmn.2004.0520107

Sauter, D., Cannat, M., Rouméjon, S., Andreani, M., Birot, D., Bronner, A., et al. (2013). Continuous Exhumation of Mantle-Derived Rocks at the Southwest Indian Ridge for 11 Million Years. *Nat. Geosci.* 6 (4), 314–320. doi:10.1038/ngeo1771

Sawyer, D. S., Whitmarsh, R. B., and Klaus, A. (1994). *Proc. ODP, Init. Repts., 149.* College Station: TX (Ocean Drilling Program). doi:10.2973/odp.proc.ir.149.1994

Schlindwein, V., and Schmid, F. (2016). Mid-ocean ridge Seismicity Reveals Extreme Types of Ocean Lithosphere. *Nature* 535, 276–279. doi:10.1038/nature18277

Schmid, F., and Schlindwein, V. (2016). Microearthquake Activity, Lithospheric Structure, and Deformation Modes at an Amagmatic Ultraslow Spreading Southwest Indian Ridge Segment. *Geochem. Geophys. Geosyst.* 17 (7), 2905–2921. doi:10.1002/2016gc006271

Schulte, M., Blake, D., Hoehler, T., and McCollom, T. (2006). Serpentinization and its Implications for Life on Early Earth and Mars. *Astrobiology* 6 (2), 364–376. doi:10.1089/ast.2006.6.364

Schwarzenbach, E. M., Früh-Green, G. L., Bernasconi, S. M., Alt, J. C., and Plas, A. (2013). Serpentinization and Carbon Sequestration: a Study of Two Ancient Peridotite-Hosted Hydrothermal Systems. *Chem. Geol.* 351, 115–133. doi:10.1016/j.chemgeo.2013.05.016

Seifert, K., and Brunotte, D. (1996). "Geochemistry of Serpentinized Mantle Peridotite from Site 897 in the Iberia Abyssal plain," in *Proceedings of the Ocean Drilling Program, 149 Scientific Results*. Editors R. B. Whitmarsh, D. S. Sawyer, A. Klaus, and D. G. Masson (College Station: TX (Ocean Drilling Program)), 413–424. doi:10.2973/odp.proc.sr.149.216.1996

Seyler, M., Cannat, M., and Mével, C. (2003). Evidence for Major-Element Heterogeneity in the Mantle Source of Abyssal Peridotites from the Southwest Indian Ridge (52° to 68°E). *Geochem. Geophys. Geosyst.* 4 (2). doi:10.1029/2002gc000305

Seyler, M., Lorand, J. P., Dick, H. J. B., and Drouin, M. (2007). Pervasive Melt Percolation Reactions in Ultra-depleted Refractory Harzburgites at the Mid-Atlantic Ridge, 15°20′N: ODP Hole 1274A. *Contrib. Mineral. Petrol.* 153 (3), 303–319. doi:10.1007/s00410-006-0148-6

Silantyev, S. A., Krasnova, E. A., Cannat, M., Bortnikov, N. S., Kononkova, N. N., and Beltenev, V. E. (2011). Peridotite–gabbro–trondhjemite Association of the

Mid-Atlantic Ridge between 12°58′ and 14°45′ N: Ashadze and Logachev Hydrothermal Vent fields. *Geochem. Int.* 49 (4), 323–354. doi:10.1134/s0016702911040070

Skelton, A. D. L., and Valley, J. W. (2000). The Relative Timing of Serpentinisation and Mantle Exhumation at the Ocean–Continent Transition, Iberia: Constraints from Oxygen Isotopes. *Earth Planet. Sci. Lett.* 178 (3–4), 327–338. doi:10.1016/s0012-821x(00)00087-x

Skelton, A., Whitmarsh, R., Arghe, F., Crill, P., and Koyi, H. (2005). Constraining the Rate and Extent of Mantle Serpentinization from Seismic and Petrological Data: Implications for Chemosynthesis and Tectonic Processes. *Geofluids* 5 (3), 153–164. doi:10.1111/j.1468-8123.2005.00111.x

Sleep, N. H., Meibom, A., Fridriksson, T., Coleman, R. G., and Bird, D. K. (2004). H_2-rich Fluids from Serpentinization: Geochemical and Biotic Implications. *Proc. Natl. Acad. Sci.* 101 (35), 12818–12823. doi:10.1073/pnas.0405289101

Snow, J. E., and Dick, H. J. B. (1995). Pervasive Magnesium Loss by marine Weathering of Peridotite. *Geochim. Cosmochim. Acta* 59 (20), 4219–4235. doi:10.1016/0016-7037(95)00239-v

Takai, K., Nakamura, K., Toki, T., Tsunogai, U., Miyazaki, M., Miyazaki, J., et al. (2008). Cell Proliferation at 122°C and Isotopically Heavy CH_4 Production by a Hyperthermophilic Methanogen under High-Pressure Cultivation. *Proc. Natl. Acad. Sci.* 105 (31), 10949–10954. doi:10.1073/pnas.0712334105

Tamura, A., Arai, S., Ishimaru, S., and Andal, E. S. (2008). Petrology and Geochemistry of Peridotites from IODP Site U1309 at Atlantis Massif, MAR 30°N: Micro- and Macro-Scale Melt Penetrations into Peridotites. *Contrib. Mineral. Petrol.* 155 (4), 491–509. doi:10.1007/s00410-007-0254-0

Tao, C., Seyfried, W. E., Lowell, R. P., Liu, Y., Liang, J., Guo, Z., et al. (2020). Deep High-Temperature Hydrothermal Circulation in a Detachment Faulting System on the Ultra-slow Spreading ridge. *Nat. Commun.* 11 (1), 1300. doi:10.1038/s41467-020-15062-w

Toft, P. B., Arkani-Hamed, J., and Haggerty, S. E. (1990). The Effects of Serpentinization on Density and Magnetic Susceptibility: a Petrophysical Model. *Phys. Earth Planet. Inter.* 65 (1–2), 137–157. doi:10.1016/0031-9201(90)90082-9

Tolstoy, M., Harding, A. J., and Orcutt, J. A. (1993). Crustal Thickness on the Mid-Atlantic Ridge: Bull's-Eye Gravity Anomalies and Focused Accretion. *Science* 262 (5134), 726–729. doi:10.1126/science.262.5134.726

Tucholke, B. E., and Sibuet, J. C. (2007). "Leg 210 Synthesis: Tectonic, Magmatic, and Sedimentary Evolution of the Newfoundland–Iberia Rift," in *Proc. ODP, Sci. Results210*. Editors B. E. Tucholke, J. C. Sibuet, and A. Klaus (College Station: TX (Ocean Drilling Program)), 1–56. doi:10.2973/odp.proc.sr.210.101.2007

Tucholke, B. E., Sibuet, J. C., and Klaus, A. (2004). *Proc. ODP, Init.* Repts., 210. College Station: TX (Ocean Drilling Program). doi:10.2973/odp.proc.ir.210.2004

Tutolo, B. M., Seyfried, W. E., and Tosca, N. J. (2020). A Seawater Throttle on H_2 Production in Precambrian Serpentinizing Systems. *Proc. Natl. Acad. Sci.* 117 (26), 14756–14763. doi:10.1073/pnas.1921042117

Vils, F., Pelletier, L., Kalt, A., Müntener, O., and Ludwig, T. (2008). The Lithium, boron and Beryllium Content of Serpentinized Peridotites from ODP Leg 209 (Sites 1272A and 1274A): Implications for Lithium and boron Budgets of Oceanic Lithosphere. *Geochim. Cosmochim. Acta* 72 (22), 5475–5504. doi:10.1016/j.gca.2008.08.005

Vissers, R. L. M., van Hinsbergen, D. J. J., Meijer, P. Th., and Piccardo, G. B. (2013). Kinematics of Jurassic Ultra-slow Spreading in the Piemonte Ligurian Ocean. *Earth Planet. Sci. Lett.* 380, 138–150. doi:10.1016/j.epsl.2013.08.033

Whitmarsh, R. B., Beslier, M.-O., and Wallace, P. J. (1998). *Proc. ODP, Init.* Repts., 173. College Station: TX (Ocean Drilling Program). doi:10.2973/odp.proc.ir.173.1998

Whitmarsh, R. B., Manatschal, G., and Minshull, T. A. (2001). Evolution of Magma-Poor continental Margins from Rifting to Seafloor Spreading. *Nature* 413, 150–154. doi:10.1038/35093085

Whitmarsh, R. B., and Miles, P. R. (1995). Models of the Development of the West Iberia Rifted continental Margin at 40°30′N Deduced from Surface and Deep-Tow Magnetic Anomalies. *J. Geophys. Res. Sol. Earth* 100 (B3), 3789–3806. doi:10.1029/94jb02877

Whitmarsh, R. B., and Wallace, P. J. (2001). "The Rift-To-Drift Development of the West Iberia Nonvolcanic continental Margin: a Summary and Review of the Contribution of Ocean Drilling Program Leg 173," in *Proceedings of the Ocean Drilling Program, 173 Scientific Results*. Editors M.-O. Beslier, R. B. Whitmarsh, P. J. Wallace, and J. Girardeau (College Station: TX (Ocean Drilling Program)), 1–36. doi:10.2973/odp.proc.sr.173.017.2001

Whitmarsh, R. B., White, R. S., Horsefield, S. J., Sibuet, J.-C., Recq, M., and Louvel, V. (1996). The Ocean-Continent Boundary off the Western continental Margin of Iberia: Crustal Structure West of Galicia Bank. *J. Geophys. Res. Solid Earth* 101 (B12), 28291–28314. doi:10.1029/96jb02579

Williams, S. E., Whittaker, J. M., Halpin, J. A., and Müller, R. D. (2019). Australian-antarctic Breakup and Seafloor Spreading: Balancing Geological and Geophysical Constraints. *Earth Sci. Rev.* 188, 41–58. doi:10.1016/j.earscirev.2018.10.011

Wolery, T. J., and Jarek, R. L. (2003). *Software User's Manual EQ3 6, Version 8.0. Albuquerque (NM): Sandia National Laboratories*.

Wolery, T. J., and Jove-Colon, C. F. (2004). *Qualification of Thermodynamic Data for Geochemical Modeling of mineral-water Interactions in Dilute Systems*. US Department of Energy, Bechtel SAIC Company, LCC, Las Vegas (NV). doi:10.2172/850412

Zhao, X. (2001). Palaeomagnetic and Rock Magnetic Results from Serpentinized Peridotites beneath the Iberia Abyssal plain. *Geol. Soc. Spec. Pub.* 187, 209–234. doi:10.1144/gsl.sp.2001.187.01.11

Zolotov, M. Y. (2014). Formation of Brucite and Cronstedtite-Bearing mineral Assemblages on Ceres. *Icarus* 228, 13–26. doi:10.1016/j.icarus.2013.09.020

Conflict of Interest: The authors declare that the research was conducted in the absence of any commercial or financial relationships that could be construed as a potential conflict of interest.